

Banner appropriate to article type will appear here in typeset article

Reynolds number effects on turbulent flow in curved channels

Giulio Soldati¹†, Paolo Orlandi¹ and Sergio Pirozzoli¹

¹Sapienza Università di Roma, Dipartimento di Ingegneria Meccanica e Aerospaziale, via Eudossiana 18, Roma, Italy

(Received xx; revised xx; accepted xx)

In this work, we study the flow in curved channels, an archetypal configuration that allows insights into problems featuring turbulence bounded by curved walls. Besides its relevance to many engineering applications, it exhibits a rich physics due to the presence of turbulence superimposed to large-scale structures driven by centrifugal instabilities. The resulting secondary motions, which depend on the channel geometry and Reynolds number, break symmetry between the convex and the concave surface. We investigate the effects of curvature by focusing on two cases of mildly and strongly curved channel, in which shear and inertia are supposed to control the general features of the flow, respectively. For each geometry, we examine systematically the effects of the Reynolds number: we run a campaign of direct numerical simulations covering flow regimes from laminar up to moderately high value of Reynolds number – based on bulk velocity and channel height – of 87000. Our analysis pivots around the friction coefficient, which is the macroscopic observable of the flow, and explores how the large-scale structures change their shape and role on turbulence for increasing Reynolds numbers. Special attention is paid to the longitudinal large-scale structures (resembling Dean vortices), and how their dynamics of splitting and merging is influenced by curvature. In addition, we also observe and characterise transverse large-scale structures populating the convex wall of strongly curved channels, which are originated by streamwise instabilities and contribute to the negative production of turbulence kinetic energy.

Key words: Direct numerical simulation, Turbulence, Curvature

1. Introduction

Turbulence bounded by curved walls is a key aspect of various engineering applications, such as highly cambered aerofoils, turbo-machinery blades and cooling channels. In these configurations, curvature alters significantly turbulence structures, impacting friction, heat transfer and flow stability. The spatially evolving and geometry-dependent nature of these flows poses major challenges in developing a unified and comprehensive description of curvature effects on turbulence, which can be achieved by considering the time-evolving

† Email address for correspondence: giulio.soldati@uniroma1.it

curved channel flow. Direct numerical simulations (DNS) of plane channel flow led to a scientific breakthrough in the theory of wall-bounded turbulence through the pioneering work of Kim *et al.* (1987), and subsequent efforts at higher Reynolds numbers were made by Lee & Moser (2015) and by Pirozzoli *et al.* (2021) for the circular pipe flow. In a similar vein, we scrutinise the effect of the Reynolds number on flow in curved channels, with the aim of providing a benchmark dataset for Reynolds averaged Navier-Stokes (RANS) and large eddy simulations (LES) of turbulent flows over curved surfaces.

Compared to flat walls, surface curvature produces additional strain rates an order of magnitude larger than what dimensional arguments would suggest (Bradshaw & Young 1973). The laminar solution of the equations of motion indicates that curvature effects on quantities such as the friction coefficient and boundary layer thickness, δ , are of the order $O(\kappa\delta)$, where κ is the surface curvature (Patel & Sotiropoulos 1997). However, experimental measurements in turbulent flow reveal much stronger effects, underscoring the direct impact of curvature on turbulence. A crucial role is played by the onset of centrifugal instabilities that break the symmetry of the flow. Wall curvature generates a centrifugal force per unit mass, $\rho U^2/r$, where U is the mean streamwise velocity at radius r from the centre of curvature, counteracted by the radial pressure gradient, $\partial P/\partial r$. Rayleigh (1917) first investigated the stability of curved flow for an ideal fluid, showing that for flow over a concave surface the centrifugal force of the displaced fluid element is greater than the centripetal pressure gradient, leading to flow instability, whereas the reverse occurs for convex walls. This idea was later supported by experimental evidence (Wattendorf 1935; Eskinazi & Yeh 1956; Ellis & Joubert 1974). Dean (1928) showed analytically that fully developed flow between two concentric cylinders becomes unstable when the Reynolds number exceeds a critical value, which decreases as the channel curvature increases. The centrifugal instability leads to the so-called Dean vortices, pairs of counter-rotating longitudinal roll cells. Similar structures, the Taylor-Görtler vortices, form when the flow over a concave surface exceeds a critical Reynolds number (Görtler 1954). Several experiments on boundary layers over concave walls (So & Mellor 1975; Smits *et al.* 1979; Hoffmann *et al.* 1985) and on curved duct flow (Brewster *et al.* 1959; Ellis & Joubert 1974; Hunt & Joubert 1979) revealed the presence of regular spanwise variations in mean velocity and friction coefficient, which were considered evidence for the existence of longitudinal large-scale structures. Due to these stable structures, an upwash (downwash) motion is generated between a pair of counter-rotating vortices, resulting in a corresponding peak (trough) in boundary layer thickness and a trough (peak) in the friction coefficient. Other experiments (Eskinazi & Yeh 1956; Ramaprian & Shivaprasad 1978; Kobayashi *et al.* 1989), however, did not detect any variation along the span. Barlow & Johnston (1988) noted the presence of large-scale eddies, which did not cause spanwise variations due to their unsteadiness.

The dynamics of longitudinal vortices may be unsteady due to events of splitting and merging, depending on curvature and Reynolds number. Through experiments in a curved duct, Ligrani & Niver (1988) and Ligrani *et al.* (1994) observed the splitting of vortex pairs, during which new vortex pairs seem to emerge from the concave wall between existing pairs. A similar splitting mechanism was noted by Alfredsson & Persson (1989) in channels with rotation and by Matsson & Alfredsson (1990) in a channel with both curvature and rotation. Flow visualisations with reflective flakes allowed the authors to recognise the disappearance of vortex pairs from the merging of adjacent bright streaks. Guo & Finlay (1991), using linear stability theory and spectral methods, found that vortex splitting and merging in rotating or curved channels are caused by Eckhaus instability, namely a secondary instability of steady periodic flows (such as the Dean vortex flow) with respect to spanwise perturbations (Eckhaus 1965). In addition, a secondary instability with respect to streamwise perturbations affects the curved channel flow. By simulated roll cells in curved channels, Finlay *et al.* (1988) observed

a ‘wavy Dean vortex flow’ in the form of traveling waves superposed on the secondary flow (the Dean vortices). The authors suggested that traveling waves are originated by a shear-layer instability induced by the Dean vortices. Consistently, the stability analysis carried out by Yu & Liu (1991) for the Görtler flow identified the inflectional profile of the mean velocity as the mechanism driving the secondary instability. Similar results were obtained through experiments of curved channel flow by Matsson & Alfredsson (1990), who found a secondary instability of traveling-wave type at a Reynolds number about three times higher than the critical one for the primary (centrifugal) instability. The secondary instability was further characterised by Matsson & Alfredsson (1992), who described it as a ‘wave train riding on the primary instability’, traveling in the downstream direction with about 80% of the bulk velocity and with a streamwise wavelength slightly larger than the spanwise wavelength of the primary disturbance.

The distinct three-dimensional effects associated with concave curvature are absent in the case of convex curvature, whose main effect is to reduce turbulence intensity (Gillis & Johnston 1983). So & Mellor (1973) found experimentally that the turbulent stress decreases near the wall and vanishes about midway between the convex surface and the edge of the velocity gradient layer. The strong reduction in turbulent shear stress due to convex curvature leads to a shift of the zero-crossing point closer to the convex wall. This asymmetry is associated with a displacement between the locations where turbulent and viscous shear stresses vanish, creating a small region with negative production of turbulence kinetic energy. The phenomenon of negative production in curved channel flow was examined by Eskinazi & Erian (1969), who related it to a local ‘energy reversal’ mechanism, whereby energy is transferred from turbulent fluctuations to the mean flow. In the attempt to interpret the effects of curvature on the velocity profile, Patel (1969) observed an analogy between the effects of concave (convex) curvature and favorable (adverse) pressure gradient on boundary layers. That author concluded that curvature affects directly the inner layer, contrary to previous studies suggesting that the velocity profile is curvature-independent in the viscous sublayer. The analogy between the effects of curvature and streamwise pressure gradient, however, lacks general validity: a favorable pressure gradient can lead to flow relaminarisation, which may occur, rather, on the convex wall of the curved channel (Brethouwer 2022).

Despite the large amount of laboratory data available in the literature, the effects of curvature on turbulence have neither been fully quantified nor understood. Due to the narrow range of both Reynolds numbers and curvatures spanned by the experiments conducted so far, it is difficult to draw general conclusions. Additionally, it is often unclear whether the flow is fully developed, inflow conditions are free of disturbances and three-dimensional effects due to side walls are negligible. DNS is an invaluable tool that can help to understand the flow physics more thoroughly. The first major contribution was made by Moser & Moin (1987), who performed a DNS of fully developed turbulent flow at bulk Reynolds number $Re_b = u_b \delta / \nu = 5200$ (where u_b is the bulk velocity, δ the channel height and ν the kinematic viscosity) in a curved channel with curvature radius $r_c / \delta = 39.5$ at the channel centreline. They concluded that most turbulence quantities, except for the turbulent shear stress, are equivalent on the convex and concave sides of the channel when scaled in local wall units, inferring the existence of flow similarity. However, Nagata & Kasagi (2004), who carried out several DNS of mildly ($r_c / \delta = 39.5$) to moderately ($r_c / \delta = 2.5$) curved channel flow at $Re_b \approx 4600$, did not observe near-wall similarity. More recently, Brethouwer (2022) studied by DNS the fully developed turbulent flow in channels with mild ($r_c / \delta = 30$) to moderate ($r_c / \delta = 3$) curvature at $Re_b = 40000$. Velocity fluctuations in local scaling turned out to collapse into a single curve in the viscous wall region, while in the outer layer were found to depend heavily on curvature.

Given this background, with this work we aim to extend our understanding of turbulence

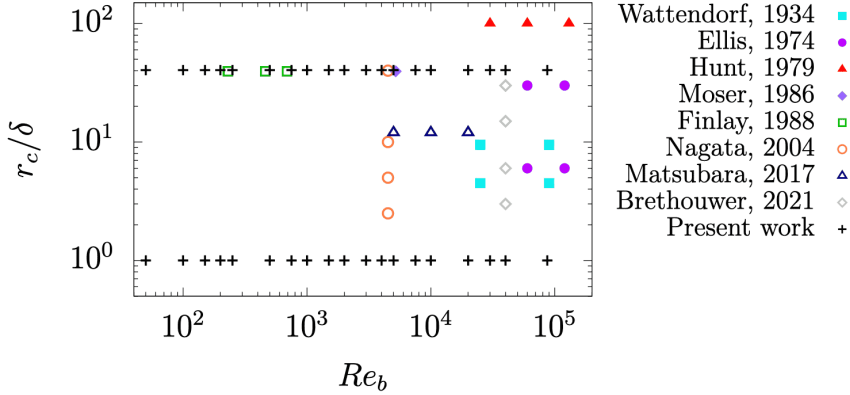


Figure 1: Overview of previous experimental and computational studies of curved channel flow in terms of bulk Reynolds number (Re_b), and relative curvature radius (r_c/δ). Crosses indicate the flow cases computed in the present work.

in curved channels by widening the range of Reynolds numbers and examining cases with extreme curvature, thus filling existing gaps in the current literature. This is well illustrated in figure 1, which reports an overview of the controlling flow parameters, namely bulk Reynolds number (Re_b) and relative curvature radius (r_c/δ), from previous experimental and computational studies of curved channel flow, along with our DNS. We investigate the effects of channel curvature by focusing on two extreme cases, namely a mildly ($r_c/\delta = 40.5$) and strongly ($r_c/\delta = 1$) curved channel. According to the definition proposed by Hunt & Joubert (1979), these two cases correspond to ‘shear-dominated’ and ‘inertia-dominated’ flows, respectively. For both cases, we examine the effect of the Reynolds number, which has never been studied systematically for this flow configuration, by carrying out a DNS campaign covering a wide range of flow regimes. Special attention is paid to friction, specifically to how the changes in flow organisation and turbulence structures induced by curvature affect its behavior. This analysis reveals important insights into the flow transition, which varies according to the type and magnitude of curvature. In addition, we focus on characterising the secondary motions induced by large-scale structures that develop in curved channel flow.

The paper is structured as follows: in §2 we describe the numerical methodology used for the analysis; in §3 we present the main results of the DNS campaign: specifically, the friction coefficient and flow transition are studied in §3.1; the flow organisation is explored through instantaneous velocity fields in §3.2 and time-averaged velocity spectra in §3.3; longitudinal large-scale structures are addressed in §3.4, with a focus on splitting and merging events in §3.5, and on their role on velocity fluctuations in §3.6; transverse large-scale structures are discussed in §3.7, and their role on shear stress and pressure fluctuations at the convex wall is analysed in §3.8; the structure of the turbulent shear stress is investigated in §3.9 through a quadrant analysis, and a region with negative production is observed and examined in §3.10; finally, in §4 we conclude with a discussion of the results.

2. Methodology

The turbulent flow in curved channels is simulated in a computational domain bounded by sectors of concentric cylinders, as shown in figure 2. The velocity components along the streamwise (θ), radial (r) and spanwise (z) directions are denoted by u , v and w , respectively. The flow is driven by a mean-pressure gradient ($\partial P/\partial \theta$), which is imposed as a volumetric

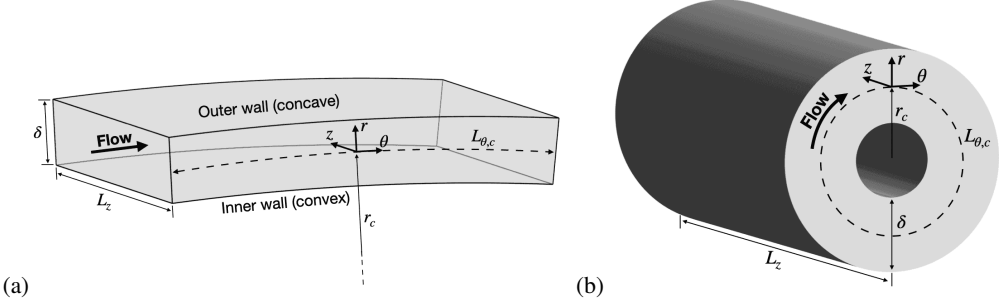


Figure 2: Computational setup for flow in mildly (a) and strongly (b) curved channels.

forcing to maintain constant mass flow rate in time. Numerical simulations are carried out assuming periodicity conditions in the streamwise and spanwise directions, so that the flow is fully developed.

The in-house code used for DNS, which solves the incompressible Navier-Stokes equations in cylindrical coordinates, stems from a previous solver developed by Verzicco & Orlandi (1996) and used for DNS of pipe flow by Orlandi & Fatica (1997). The switch from the pipe setup to the curved channel was attained implementing two main modifications to the code. The first is the addition of an inner cylinder (the inner wall of the channel) concentric to the outer cylinder. The second is the change in direction of the mean-pressure gradient, which is imposed along the azimuthal direction (θ), namely the streamwise direction of the curved channel. In this respect, we note that the pressure term in the streamwise momentum equation is $(\partial P / \partial \theta) / r$, with constant $\partial P / \partial \theta$, hence the volumetric forcing varies along the radial direction. The spatial discretisation is based on second-order finite-difference schemes, which are implemented in the classical marker-and-cell framework (Harlow & Welch 1965). The pressure is located at the cell centres, whereas the velocity components at the cell faces, thus removing odd-even decoupling phenomena and guaranteeing discrete conservation of the total kinetic energy in the inviscid limit (Pirozzoli 2023). The governing equations are advanced in time by means of a hybrid third-order low-storage Runge-Kutta algorithm, whereby the diffusive terms are handled implicitly and convective terms explicitly. Further details regarding the numerical methods implemented in the code can be found e.g. in Pirozzoli *et al.* (2021). The code was adapted to run on clusters of graphic accelerators (GPUs), using a combination of CUDA Fortran and OpenACC directives, and relying on the CUDA libraries for efficient execution of fast Fourier transforms.

The flow field is controlled by two parameters, namely the bulk Reynolds number, Re_b , and the radius of curvature at the centreline, r_c / δ . To investigate the effect of both parameters, we split the simulation campaign in two main groups: 1) shear-dominated flow with mild curvature ($r_c / \delta = 40.5$), and 2) inertia-dominated with strong curvature ($r_c / \delta = 1$). Throughout the paper, we will refer to the first group as R40 and to the second group as R1. Within each group, we vary the Reynolds number from $Re_b = 25$ up to 87000. The domain extends in the radial direction from $r = r_i$ (inner wall), to $r = r_o$ (outer wall), where $r_o - r_i = \delta$ and $r_c = (r_i + r_o) / 2$. To compare cases with different values of the curvature radius, we consider the y -coordinate, aligned with the radial direction and origin shifted at the inner wall, i.e. $y = r - r_i$. In all cases, the computational domain has a streamwise length $L_\theta / \delta = 2\pi$ along the centreline, meaning that for the R1 cases the domain resolves a full cylinder circumference (see figure 2). The spanwise width is set to $L_z / \delta = 4$ for the R40 cases, and it is doubled for R1 cases, in order to minimise the influence of spanwise periodicity on the large-scale structures. The effects of the domain sizes on the simulations results are

Mild curvature (R40): $r_c/\delta = 40.5$, $L_\theta/\delta \times L_z/\delta = 2\pi \times 4$					
Re_b	$Re_{\tau,i}$	$Re_{\tau,o}$	$N_\theta \times N_r \times N_z$	$r_o\Delta\theta^+ \times \Delta r^+ \times \Delta z^+$	
25	6	6	$129 \times 65 \times 129$	$0.6 \times 0.01 \times 0.4$	
50	9	9	$129 \times 65 \times 129$	$0.9 \times 0.01 \times 0.5$	
100	12	12	$129 \times 65 \times 129$	$1.2 \times 0.01 \times 0.8$	
150	15	15	$129 \times 65 \times 129$	$1.5 \times 0.01 \times 0.9$	
200	17	17	$129 \times 65 \times 129$	$1.7 \times 0.01 \times 1.0$	
250	19	19	$129 \times 65 \times 129$	$1.9 \times 0.01 \times 1.2$	
500	28	31	$129 \times 65 \times 129$	$3.1 \times 0.01 \times 2.0$	
750	35	40	$129 \times 65 \times 129$	$4.0 \times 0.02 \times 2.5$	
1000	41	50	$129 \times 65 \times 129$	$5.0 \times 0.01 \times 3.1$	
1500	51	65	$161 \times 97 \times 161$	$5.2 \times 0.01 \times 3.2$	
2000	61	78	$193 \times 97 \times 193$	$5.2 \times 0.01 \times 3.3$	
2500	69	92	$225 \times 97 \times 225$	$5.3 \times 0.02 \times 3.3$	
3000	82	112	$257 \times 129 \times 257$	$5.6 \times 0.01 \times 3.5$	
4000	103	143	$321 \times 129 \times 321$	$5.8 \times 0.01 \times 3.6$	
5000	139	170	$321 \times 145 \times 353$	$6.8 \times 0.01 \times 3.8$	
7500	211	241	$449 \times 145 \times 449$	$6.9 \times 0.02 \times 4.3$	
10000	270	305	$513 \times 161 \times 513$	$7.7 \times 0.02 \times 4.8$	
20000	506	583	$769 \times 205 \times 1025$	$9.8 \times 0.03 \times 4.6$	
30000	720	839	$1153 \times 261 \times 1537$	$9.4 \times 0.03 \times 4.4$	
40000	922	1085	$1409 \times 303 \times 1793$	$9.9 \times 0.03 \times 4.8$	
87000	1824	2177	$3073 \times 489 \times 3585$	$9.1 \times 0.03 \times 4.8$	
Strong curvature (R1): $r_c/\delta = 1.0$, $L_\theta/\delta \times L_z/\delta = 2\pi \times 8$					
Re_b	$Re_{\tau,i}$	$Re_{\tau,o}$	$N_\theta \times N_r \times N_z$	$r_o\Delta\theta^+ \times \Delta r^+ \times \Delta z^+$	
25	8	5	$129 \times 65 \times 129$	$0.8 \times 0.01 \times 0.7$	
50	11	8	$129 \times 65 \times 129$	$1.1 \times 0.01 \times 1.0$	
75	14	10	$129 \times 65 \times 129$	$1.5 \times 0.01 \times 1.3$	
100	16	12	$129 \times 65 \times 129$	$1.8 \times 0.01 \times 1.5$	
150	20	15	$129 \times 65 \times 129$	$2.2 \times 0.01 \times 1.9$	
200	23	18	$129 \times 65 \times 129$	$2.6 \times 0.01 \times 2.2$	
250	26	21	$129 \times 65 \times 129$	$3.0 \times 0.01 \times 2.6$	
500	39	35	$129 \times 65 \times 129$	$5.1 \times 0.01 \times 4.4$	
750	49	47	$161 \times 65 \times 193$	$5.5 \times 0.02 \times 3.9$	
1000	58	58	$193 \times 97 \times 257$	$5.7 \times 0.01 \times 3.6$	
1500	73	79	$225 \times 97 \times 289$	$6.7 \times 0.01 \times 4.4$	
2000	86	98	$225 \times 129 \times 385$	$8.2 \times 0.01 \times 4.0$	
2500	98	115	$289 \times 129 \times 449$	$7.6 \times 0.01 \times 4.1$	
3000	110	132	$385 \times 129 \times 513$	$6.5 \times 0.01 \times 4.1$	
4000	132	165	$449 \times 145 \times 513$	$6.9 \times 0.01 \times 5.1$	
5000	152	193	$449 \times 145 \times 769$	$8.1 \times 0.02 \times 4.0$	
7500	199	263	$577 \times 145 \times 961$	$8.6 \times 0.02 \times 4.4$	
10000	244	327	$641 \times 161 \times 1153$	$9.6 \times 0.04 \times 4.5$	
20000	403	563	$1153 \times 205 \times 2049$	$9.2 \times 0.03 \times 4.4$	
30000	551	784	$1665 \times 261 \times 2817$	$8.8 \times 0.02 \times 4.4$	
40000	697	995	$2049 \times 303 \times 3585$	$9.2 \times 0.02 \times 4.4$	
87000	1362	1952	$4097 \times 489 \times 7169$	$9.0 \times 0.02 \times 4.4$	

Table 1: Flow parameters: bulk Reynolds number, friction Reynolds number at the inner and outer wall, number of grid points and grid spacing in inner units in the streamwise, radial and spanwise directions, respectively. The title line reports curvature radius and domain extension in the streamwise (along the centreline) and spanwise directions.

assessed in appendix A. Domain sizes, number of grid points and grid spacings are listed in table 1, along with the resulting friction Reynolds number at the inner ($Re_{\tau,i} = u_{\tau,i}\delta/2\nu$) and outer wall ($Re_{\tau,o} = u_{\tau,o}\delta/2\nu$). Distinction between inner and outer wall is necessary as the friction velocity changes depending on the wall at which it is evaluated. A global friction velocity can also be defined based on the mean-pressure gradient, as shown in previous works (e.g. Moser & Moin 1987; Brethouwer 2022). Inner, outer and global friction velocities are defined respectively as

$$u_{\tau,i} = \sqrt{\nu \frac{\partial U}{\partial r} \Big|_{r_i}}, \quad u_{\tau,o} = \sqrt{\nu \frac{\partial U}{\partial r} \Big|_{r_o}}, \quad u_{\tau,g} = \sqrt{\frac{u_{\tau,i}^2 r_i^2 + u_{\tau,o}^2 r_o^2}{2r_c^2}}, \quad (2.1)$$

where $u_{\tau,g}$ is derived in appendix B.

Throughout the paper, we will use two types of normalisation: local wall scaling, based on $u_{\tau,i}$ and $u_{\tau,o}$ (denoted with the ‘plus’ superscript), and global wall scaling, based on $u_{\tau,g}$ (denoted with the ‘star’ superscript). Brackets denote the averaging operator (where the subscripts denote the variables over which the averaging is done), the overline is reserved for temporal averages, capital letters denote flow properties averaged in the homogeneous spatial directions and in time, and lower-case letters denote instantaneous values. Hence, $u = U + u'$, where u' is the fluctuation from the mean. The grid spacings in local wall scaling ($r_o\Delta\theta^+$ and Δr_o^+) listed in table 1 are evaluated at the outer wall, which is the most critical as the wall shear stress is higher and the grid spacing in the streamwise direction is larger. All simulations are run for sufficient time to reach a statistically steady state, and further for at least $600\delta/u_b$ to ensure convergence of statistics, which is verified in appendix C.

3. Results

3.1. Friction coefficient and flow transition

The friction coefficient is a key parameter for characterising the transition from laminar to turbulent flow in curved channels. According to the various definitions of friction velocity given in (2.1), we define local friction coefficients at the inner and at the outer wall, as well as a global friction coefficient, namely

$$C_{f,i} = 2 \left(\frac{u_{\tau,i}}{u_b} \right)^2, \quad C_{f,o} = 2 \left(\frac{u_{\tau,o}}{u_b} \right)^2, \quad C_{f,g} = 2 \left(\frac{u_{\tau,g}}{u_b} \right)^2. \quad (3.1)$$

The global friction, based on $u_{\tau,g}$, is related to the mean-pressure gradient (B 3), hence it is useful for comparing the power required to drive the flow in a curved channel versus a plane channel. In the inset of figure 3 we show the global friction coefficient (circles) as a function of the bulk Reynolds number, which can be compared with the friction coefficient of a plane channel in the laminar regime, $C_f = 12/Re_b$ (dashed line), and in the turbulent regime via the logarithmic friction relation,

$$\sqrt{\frac{2}{C_f}} = \frac{1}{k} \left[\ln \left(\frac{Re_b}{2} \sqrt{\frac{C_f}{2}} \right) - 1 \right] + A \quad (3.2)$$

(solid line), obtained by Zanoun *et al.* (2009) from the logarithmic law of the wall, where the log-law constants are $k = 0.41$ and $A = 5.17$. For the R40 flow cases (a) the global friction coefficient is nearly equivalent to that of a plane channel at the same Reynolds number both in the laminar and turbulent regime, whereas for the R1 flow cases (b) it is slightly higher, especially in the transitional regime ($500 \leq Re_b \leq 3000$). This indicates that frictional resistance in curved channel flows is only moderately higher than in plane channel flow,

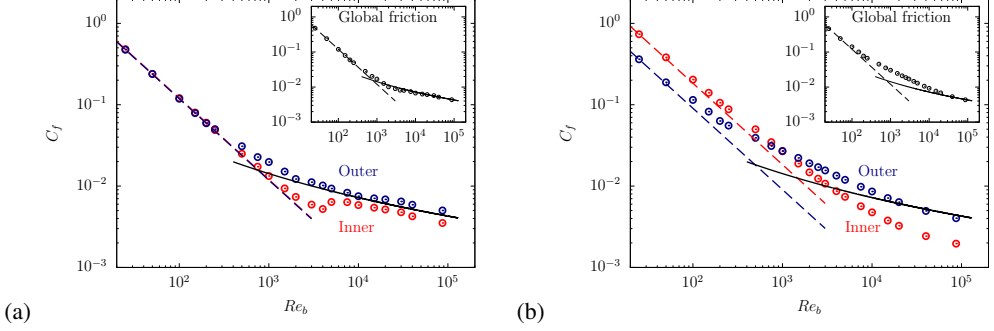


Figure 3: Friction coefficient as a function of the bulk Reynolds number for the R40 flow cases (a) and R1 flow cases (b). Red circles denote the local friction coefficient at the inner wall ($C_{f,i}$), blue circles at the outer wall ($C_{f,o}$), black circles denote in the insets the global friction coefficient ($C_{f,g}$); dashed lines denote the analytical friction law for laminar flow (red for the convex wall, blue for the concave wall, black for the plane channel), black solid lines the logarithmic friction relation for plane channel flow (3.2).

consistent with previous experimental (Wattendorf 1935) and computational (Brethouwer 2022) results.

In figure 3 we show the local friction coefficient at the two walls as a function of the bulk Reynolds number. In the turbulent regime, friction at the outer wall is always higher than at the inner wall, due to increased turbulence intensity. For the R40 flow cases (a), the friction coefficient of a plane channel at the same Reynolds number (black solid line) is about halfway between the values at the two walls of the curved channel. For the R1 flow cases (b), the outer-wall friction matches that of an equivalent plane channel, and the inner-wall friction is significantly lower. To comment more clearly on the friction trend, especially in the laminar and transitional regime, it is useful to consider the mean velocity profiles at representative Reynolds numbers, as reported in figure 4. At sufficiently low Reynolds number, the flow in a curved channel is laminar and the velocity profile can be derived analytically as

$$U(r) = \alpha r - \frac{\beta}{r} - r \ln r, \quad (3.3)$$

where

$$\alpha = \frac{r_o^2 \ln r_o - r_i^2 \ln r_i}{r_o^2 - r_i^2}, \quad \beta = \frac{r_i^2 r_o^2 \ln(r_o/r_i)}{r_o^2 - r_i^2}. \quad (3.4)$$

For the R40 flow cases, the laminar velocity profile is nearly identical to the parabolic profile of plane channel flow, meaning that the shear stress distribution is almost symmetrical. As the curvature increases, the pressure gradient in the radial direction becomes stronger and the location of maximum velocity shifts towards the inner wall. As a result, the shear stress at the inner wall is greater than at the outer. In the laminar regime, the friction coefficient at the two walls can be determined analytically by differentiating equation (3.3), which yields

$$\frac{dU(r)}{dr} = \alpha + \frac{\beta}{r^2} - \ln r - 1. \quad (3.5)$$

For the R40 flow cases, we find $C_{f,i} \approx 12.03/Re_b$, hence nearly identical to plane Poiseuille flow, and $C_{f,o} \approx 11.83/Re_b$. In contrast, for the R1 flow cases the friction coefficient at the inner wall, $C_{f,i} \approx 18.34/Re_b$, is about twice that at the outer wall, $C_{f,o} \approx 9.04/Re_b$. Flow transition occurs when the Reynolds number reaches the critical value, which we define as the point where the friction coefficient deviates from the laminar trend by at least 1%. For

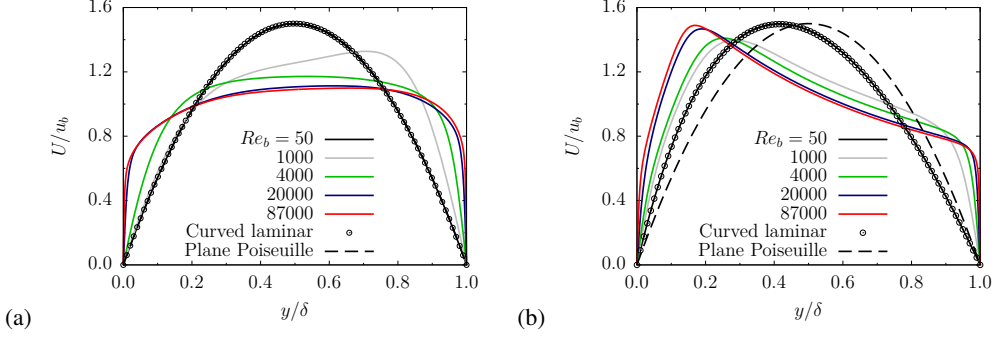


Figure 4: Mean streamwise velocity (U/u_b) at various Reynolds numbers for the R40 flow cases (a) and R1 flow cases (b). Black dashed lines refer to the Poiseuille profile, black circles to the analytical profile of laminar curved channel flow (3.3).

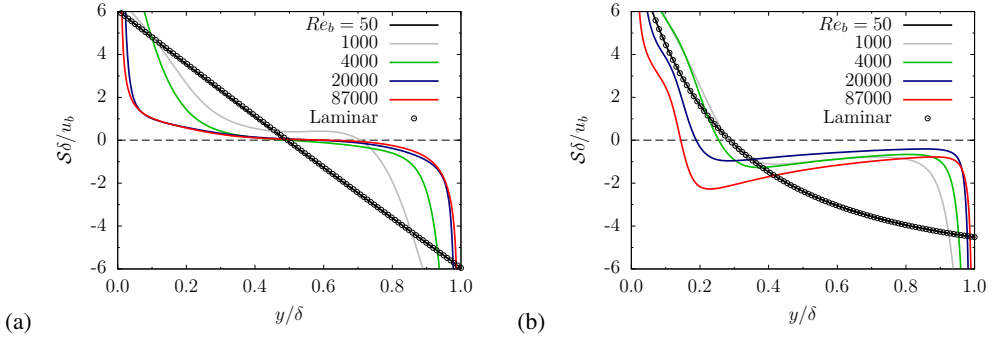


Figure 5: Mean shear rate ($S\delta/u_b$) at various Reynolds numbers for the R40 flow cases (a) and R1 flow cases (b). Circles denote the analytical profile for the laminar case.

the R40 flow cases the critical Reynolds number is $Re_b \approx 250$, which is in good agreement with the value of 228.5 found by Finlay *et al.* (1988), whereas for the R1 flow cases transition starts earlier at $Re_b \approx 50$. The transitional regime is greatly affected by curvature, depending both on its radius and on its type, with convex curvature (inner wall) tending to stabilise the flow, and concave curvature (outer wall) having the opposite effect. This is particularly evident in the R40 flow cases: at $Re_b = 1000$, the flow near the inner wall is laminar, as visible from the mean velocity profile in figure 4(a). In contrast, near the outer wall secondary motions are generated, which result in stronger momentum exchange. The peak velocity then shifts towards the outer wall, resulting in higher friction. At $Re_b = 4000$, the flow near the outer wall is fully turbulent (as will be shown later through flow visualisations), whereas the velocity profile near the inner wall is still close to the laminar state. Hence, mild convex curvature tends to delay transition compared to the plane channel, in which configuration the flow at $Re_b \approx 2600$ is close to fully turbulent (Yimprasert *et al.* 2021). By increasing the Reynolds number to 5000, the flow near the inner wall undergoes abrupt transition to a fully turbulent state, as indicated by the jump in the friction trend indicated by red circles in figure 3(a). This type of transition from laminar to turbulent regime is typical of canonical wall flows (see e.g. Patel & Head 1969), yet it is profoundly different from that at the outer wall, where transition is facilitated by centrifugal instabilities and occurs more smoothly.

For the R1 flow cases, friction in the laminar regime is higher at the inner wall. By increasing the Reynolds number, the velocity profiles tend to flatten at the outer wall, where friction increases. Turbulence is inhibited near the inner wall, and friction deviates less

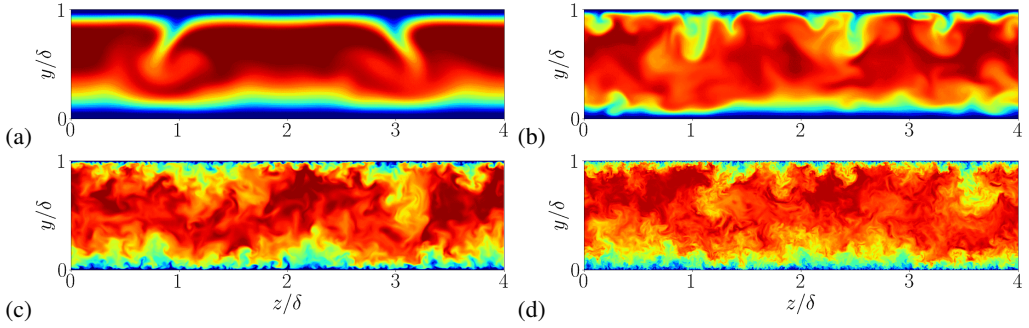


Figure 6: Instantaneous streamwise velocity fields in a cross-stream plane for the R40 flow cases at $Re_b = 1000$ (a), 4000 (b), 20000 (c), 87000 (d).

markedly from the laminar trend. An inversion occurs past $Re_b \approx 1000$, whereby friction at the outer wall becomes higher than that at the inner wall. Flow transition is facilitated by strong channel curvature, and it occurs smoothly at both walls. At the outer wall, the different transition from canonical wall flows is due to centrifugal (primary) instabilities. As we will show, in the R1 flow cases secondary motions associated with centrifugal instabilities do not reach the inner wall, and transition is affected by streamwise (secondary) instabilities, which lead to the formation of large-scale cross-stream structures.

In figure 5 we show the mean shear rate, $\mathcal{S} = dU/dr - U/r$. Similar to the case of the plane channel, the location where the mean shear vanishes defines a bound for the regions of influence of the two walls. For the R40 flow cases (a) the shear rate profile is nearly symmetrical, hence this location coincides roughly with the channel centreline, with exception of the case $Re_b = 1000$, for which it occurs at $y/\delta \approx 0.71$. In contrast, for the R1 flow cases (b) the shear rate profile is strongly asymmetrical, and the point where $\mathcal{S} = 0$ shifts towards the inner wall, between $y/\delta \approx 0.22$ and $y/\delta \approx 0.14$, moving closer to the inner wall for higher Reynolds numbers. Hence, the region of influence of the inner wall is much narrower than for the outer wall. The shear rate profile also exhibits a local maximum near the outer wall and a local minimum near the inner wall, corresponding to inflectional points of the mean velocity profiles. The local minimum near the inner wall is especially pronounced, showcasing the presence of a shear layer that can support inflectional instabilities.

3.2. Flow visualisations

The previous discussion on flow transition can be visualised through the instantaneous fields of streamwise velocity in cross-stream and wall-parallel planes, shown in figures 6 and 7 for the R40 flow cases and in figures 8 and 9 for R1 flow cases.

As for the R40 flow cases, the cross-stream and longitudinal planes at $Re_b = 1000$, shown in figures 6(a) and 7(a), highlight the onset of two symmetric large-scale ejections carrying low-speed fluid from the outer wall towards the channel core. These secondary motions are generated by two pairs of counter-rotating roll cells, which resemble closely Dean vortices. The inner-wall flow region is almost unaffected by these vortices, as one can see from figure 7(b). Figures 6(b) and 7(c), depicting the cross-stream and longitudinal planes at $Re_b = 4000$, show that fine-scale ejections and organised structures of momentum streaks characterise the outer wall, from which one can infer that the flow is fully turbulent. Traces of the longitudinal vortices appear as longitudinal bands of high-speed fluid near the inner wall, as visible in figure 7(d). Being centrifugally stable, the inner-wall flow region is still transitional, as no clear signs of turbulent activity appear. The cross-stream planes at $Re_b = 20000$ and 87000 (panels (c) and (d) of figure 6) show clear signs of streaky patterns at

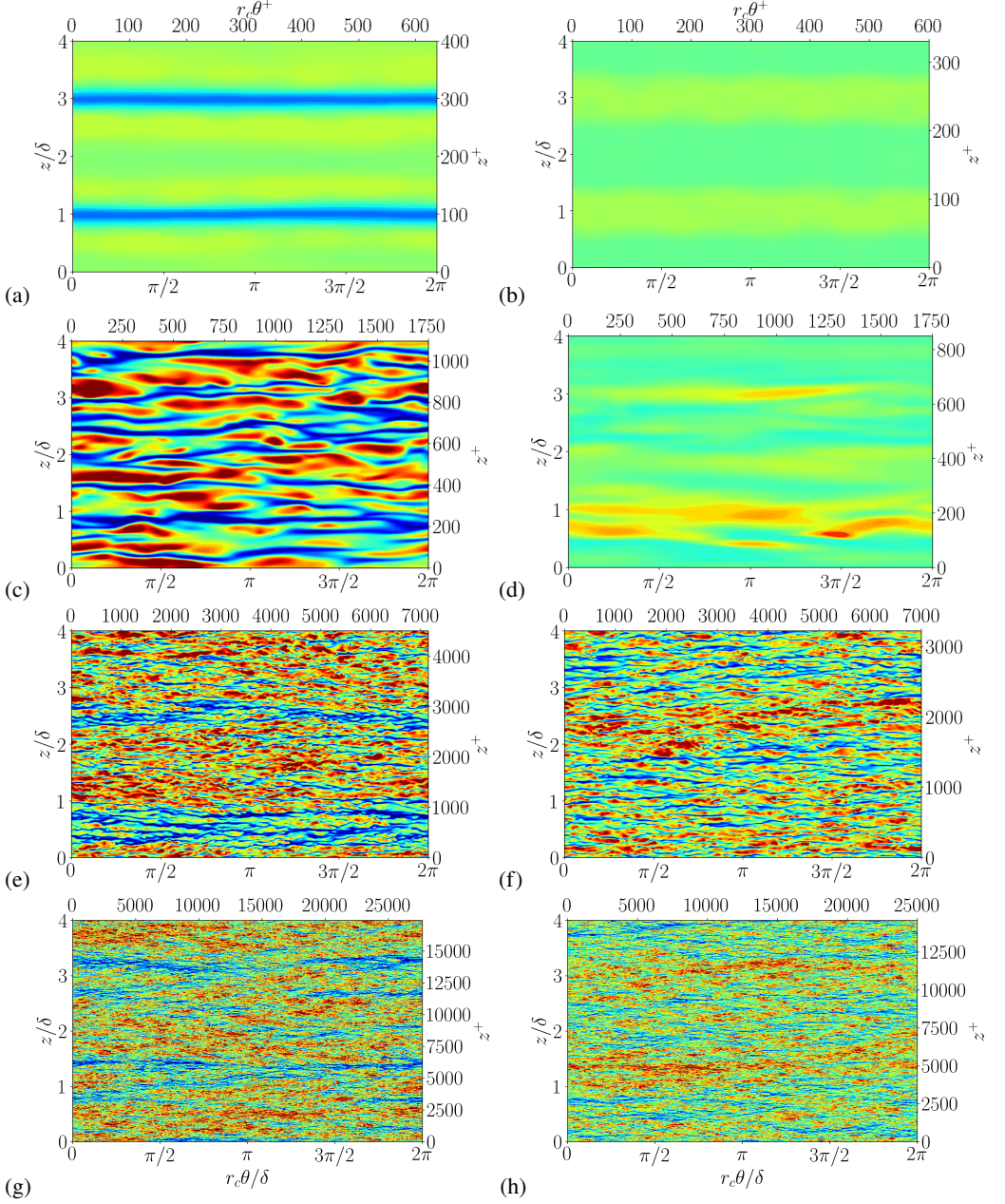


Figure 7: Instantaneous fields of streamwise velocity fluctuations for the R40 flow cases in wall-parallel planes near the outer (left panels) and inner wall (right panels) at $y^+ \approx 12$. From top to bottom, the panels correspond to $Re_b = 1000$ (a, b), 4000 (c, d), 20000 (e, f), 87000 (g, h). Streamwise and spanwise coordinates are shown in both outer units ($r_c\theta/\delta$, z/δ), and local wall units ($r_c\theta^+$, z^+). Mean flow goes from left to right.

both walls. Overlaying the small scales of turbulence, longitudinal large-scale structures are found near the outer wall, whose footprint appears in the wall-parallel planes of figures 7(e) and 7(g) as wide regions of alternating high and low speed fluid. These large-scale regions fill the entire streamwise extent of the domain, and their spanwise width is comparable with

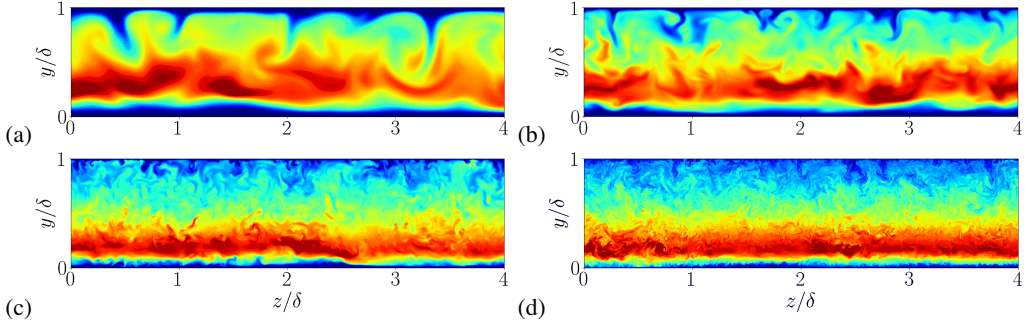


Figure 8: Instantaneous streamwise velocity fields in a cross-stream plane for the R1 flow cases at $Re_b = 1000$ (a), 4000 (b), 20000 (c), 87000 (d). Only half of the domain is shown.

the channel height, hence two pairs of roll cells are present. The influence of the latter is found to extend to the inner wall at high Reynolds numbers. In fact, low-speed regions at the outer wall, corresponding to large-scale ejections, are found at the same spanwise location as high-speed regions at the inner wall, corresponding to large-scale sweeps (panels (f) and (h) of figure 7).

Cross-stream visualisations (figure 8) show clearly how the region with higher momentum shifts towards the inner wall for the R1 flow cases, as expected from the mean velocity profiles (figure 4). As well as for the R40 flow cases, signatures of longitudinal roll cells are visible as large-scale ejections from the outer wall, although those are more numerous and chaotic. As displayed in the wall-parallel plane of figure 9(a), streaky structures appear to be quite distinct at the outer wall at $Re_b = 1000$, confirming that increasing curvature promotes the transition to turbulence. Panels (c), (e), (g) of figure 9 show that momentum streaks are less regular at the outer wall and form ripples along the streamwise direction. Furthermore, streaks are wider for the R1 flow cases than for R40, whereas the longitudinal large-scale structures are smaller and more chaotic. This makes the distinction between fine-scale turbulence and large-scale structures less clear-cut. In fact, longitudinal roll cells do not clearly show up in the wall-parallel planes of fluctuating streamwise velocity, however this does not convey that they are absent, as secondary motions due to longitudinal vortices mainly affect the wall-normal and spanwise velocity components. As visible from the wall-parallel planes shown in panels (b), (d), (f) of figure 9, the inner-wall flow region is devoid of turbulent structures, or nearly so for the highest Reynolds number (h), whereas it is characterised by the presence of large-scale structures stretched in the spanwise direction. The latter are visible in the form of alternating regions of high and low speed fluid spanning the transverse direction with spanwise width comparable with δ . The streamwise extent of each pair of transverse structures is about $\pi\delta$, meaning that the computational domain can fit two pairs, with exception of the case $Re_b = 4000$ at which the streamwise wavelength seems slightly shorter.

3.3. Velocity spectra

A clearer understanding of the energetic relevance of the various scales of motions can be achieved from inspecting the spectra of the velocity fluctuations. Spectra of both streamwise and wall-normal velocity fluctuations are presented, the former to detect large-scale structures typical of plane channel flows (Lee & Moser 2015), whereas the latter are instrumental to reveal the presence of longitudinal roll cells (Dai *et al.* 2016). Figures 10 and 11 display the pre-multiplied spectra of streamwise velocity fluctuations in the spanwise ($k_z^* E_{uu}^*$) and streamwise ($k_\theta^* E_{uu}^*$) directions at various wall-normal locations for R40 and R1 flow cases,

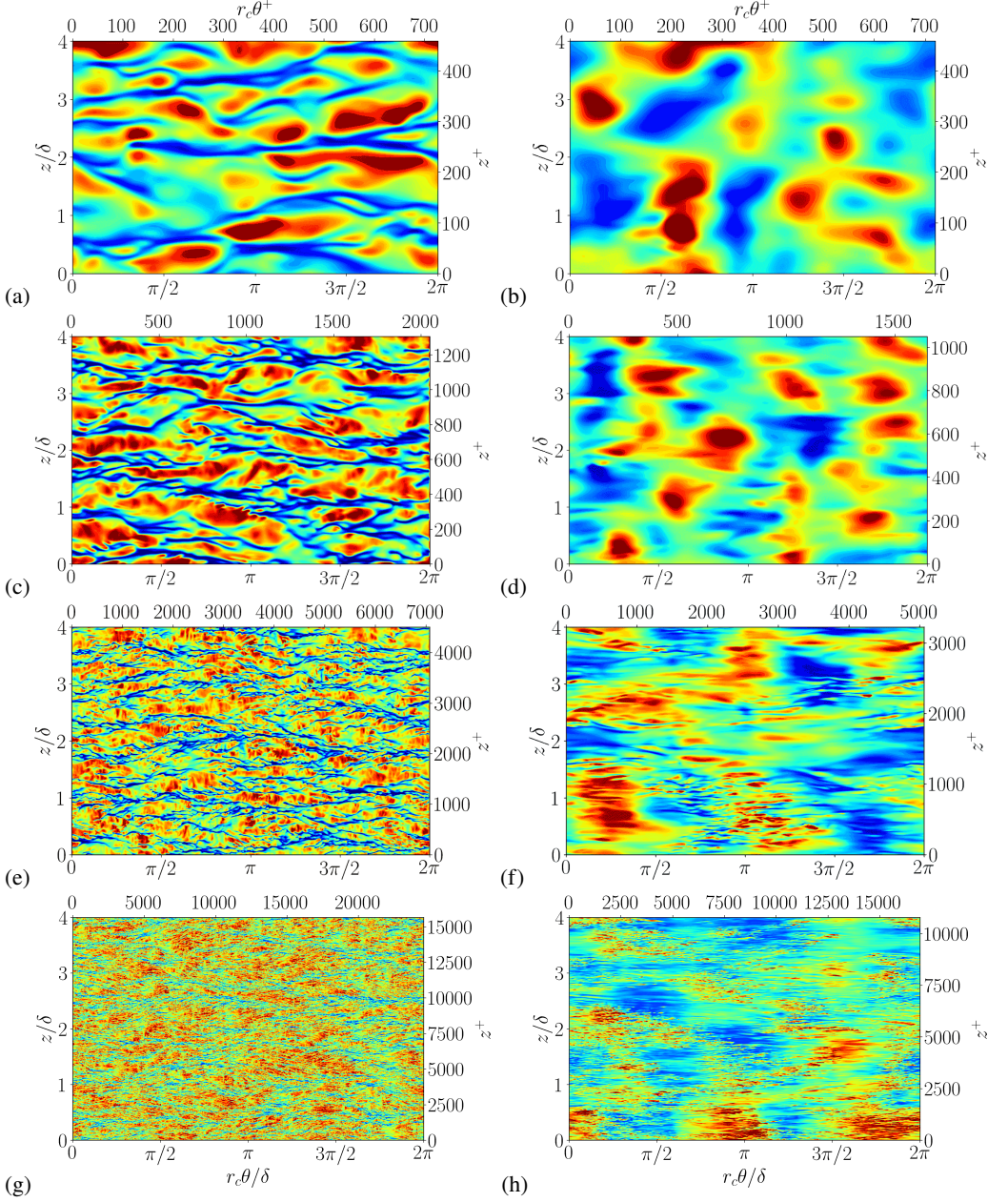


Figure 9: Instantaneous fields of streamwise velocity fluctuations for the R1 flow cases in wall-parallel planes near the outer (left panels) and inner wall (right panels) at $y^+ \approx 12$. From top to bottom, the panels correspond to $Re_b = 1000$ (a, b), 4000 (c, d), 20000 (e, f), 87000 (g, h). Streamwise and spanwise coordinates are shown in both outer units ($r_c\theta/\delta$, z/δ), and local wall units ($r_c\theta^+$, z^+). Only half of the domain is shown.

respectively. For clarity, we refer to the distance from the inner wall as y_i/δ (where $y_i/\delta = y/\delta$) and from the outer wall as y_o/δ (where $y_o/\delta = 1 - y/\delta$), both reported on the left vertical axis. The distance from the inner and outer wall is also reported on the right vertical axis in local wall units, y_i^+ and y_o^+ , respectively.

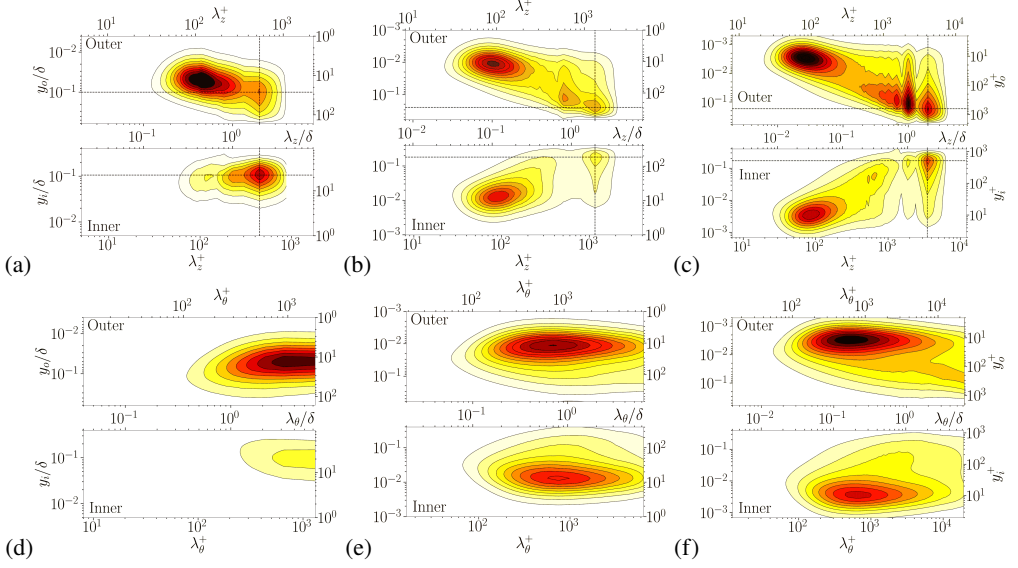


Figure 10: Pre-multiplied spectra of streamwise fluctuating velocity as a function of spanwise wavelength ($k_z^* E_{uu}^*$, upper panels) and of streamwise wavelength ($k_\theta^* E_{uu}^*$, lower panels) as the wall distance varies for the R40 flow cases. From left to right, the panels correspond to $Re_b = 4000$ (a, d), 20000 (b, e), 87000 (c, f). Wall distance from the inner and outer wall, spanwise and streamwise wavelengths are reported in outer units (y_i/δ , y_o/δ , λ_z/δ , λ_θ/δ), and in local wall units (y_i^+ , y_o^+ , λ_z^+ , λ_θ^+), respectively. Dashed lines mark wavelength and wall distance of the energy peak associated with longitudinal large-scale structures.

In the R40 flow cases a primary energy peak appears in the spanwise spectra (upper panels) near both walls at $y_i^+ \approx y_o^+ \approx 12$, $\lambda_z^+ \approx 100$, which is the typical signature of the regeneration cycle of momentum streaks (Hamilton *et al.* 1995). An exception is the case at $Re_b = 4000$: the inner-wall primary peak is nearly absent, confirming the inferences from flow visualisations. From the streamwise spectra (lower panels) we note that the streaks-related peak is at $\lambda_\theta^+ \approx 800$, meaning that the mean wavelength of momentum streaks is slightly shorter than the typical value of plane channel flows, namely $\lambda_x^+ \approx 1000$ (Monty *et al.* 2009). A secondary peak appears in the spanwise spectra farther from walls, at approximately $y_i/\delta \approx y_o/\delta \approx 0.1$ at $Re_b = 4000$ (a) and $y_i/\delta \approx y_o/\delta \approx 0.2$ at $Re_b = 20000$ (b) and 87000 (c). As seen from the intersection of the dashed lines, the energy of the peaks is concentrated at $\lambda_z/\delta \approx 2$. If the domain contains n pairs of roll cells, we expect to find a peak in the spanwise spectra at $\lambda_z = L_z/n$, where $L_z = 4\delta$ for the R40 flow cases. Flow visualisations indeed revealed the presence $n = 2$ roll cells pairs, hence we interpret these peaks as the footprint of longitudinal large-scale structures. A third peak at $\lambda_z/\delta \approx 1$ appears faintly at $Re_b = 20000$, and sharply emerges at $Re_b = 87000$. This peak corresponds to $n = 4$ pairs of longitudinal cells, indicating that roll cells with various sizes could be present, which we will investigate below. The streamwise spectra reveal that the scales of motion with the maximum streamwise wavelength, $\lambda_\theta = L_\theta = 2\pi$, are quite energetic, suggesting that the longitudinal vortices span the whole domain along the streamwise direction.

As for the R1 flow cases (figure 11) the primary peak in the spanwise spectra due to momentum streaks still occurs near the outer wall at $y_o^+ \approx 12$ (upper panels). As noted from flow visualisations, streaky structures have a greater spanwise wavelength than the R40 flow cases, which is about $\lambda_z^+ \approx 120$. Their streamwise wavelength is instead shorter, about $\lambda_\theta^+ \approx$

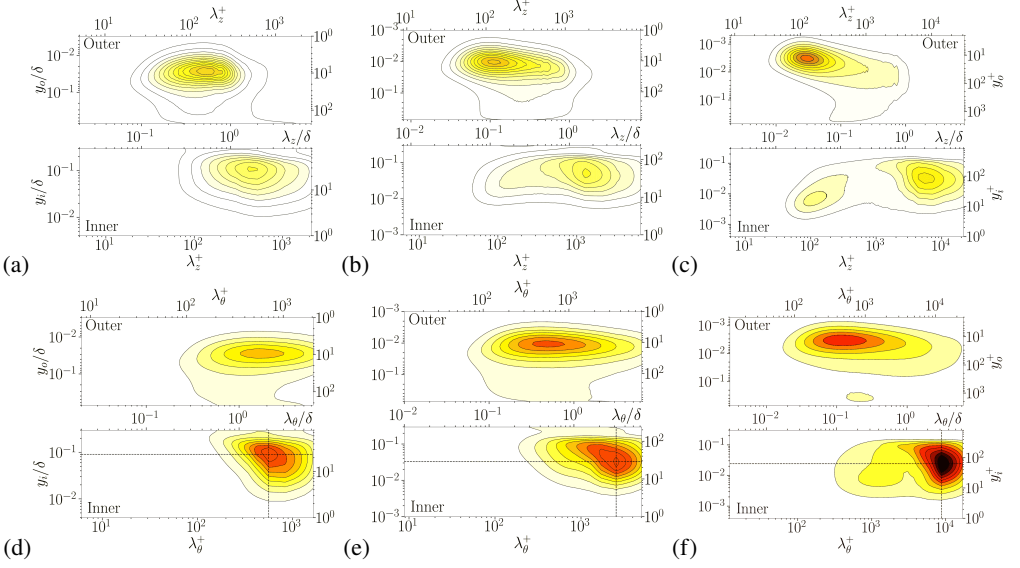


Figure 11: Pre-multiplied spectra of streamwise fluctuating velocity as a function of spanwise wavelength ($k_z^+ E_{uu}^*$, upper panels) and of streamwise wavelength ($k_\theta^+ E_{uu}^*$, lower panels) as the wall distance varies for the R1 flow cases. From left to right, the panels correspond to $Re_b = 4000$ (a, d), 20000 (b, e), 87000 (c, f). Wall distance from the inner and outer wall, spanwise and streamwise wavelengths are reported in outer units (y_i/δ , y_o/δ , λ_z/δ , λ_θ/δ), and in local wall units (y_i^+ , y_o^+ , λ_z^+ , λ_θ^+), respectively. Dashed lines mark wavelength and wall distance of the energy peak associated with transverse large-scale structures.

500, as visible from the streamwise spectra (lower panels). Near the inner wall the picture is different: the primary near-wall peak in the spanwise spectra is absent at $Re_b = 4000$ (d), starts to form at $Re_b = 20000$ (e), and only becomes visible at $Re_b = 87000$ (f). This trend, which is also found in the streamwise spectra, suggests that the inhibiting effect of convex curvature on turbulence is experienced more strongly at low Reynolds number. In contrast to the R40 flow cases, never does a secondary peak emerge in the spanwise spectra near the outer wall. This implies that the longitudinal roll cells, if present, have a negligible effect on the streamwise velocity fluctuations. A secondary peak is instead present near the inner wall at $\lambda_z/\delta \approx 2$, which moves closer to the wall (in δ units) as Re_b increases. This peak cannot be related to longitudinal roll cells for two reasons: 1) they are most intense at the outer wall, yet no secondary peak is detected there, and 2) the spanwise wavelength of longitudinal vortices must be shorter, as one can infer from figure 8 and as we will show more clearly below. To elaborate further, we consider the streamwise energy spectra, which highlight energetic modes near the inner wall at long wavelengths: $\lambda_\theta/\delta \approx 2\pi/3$ at $Re_b = 4000$ (d) and $\lambda_\theta/\delta \approx \pi$ at 20000 (e) and 87000 (f), as marked by the dashed lines. These energy peaks cannot be related neither to turbulence structures, which are absent or strongly inhibited near the inner wall, neither to longitudinal roll cells, as we have just seen through the spanwise spectra that they do not affect streamwise velocity fluctuations. However, flow visualisations in wall-parallel planes near the inner wall (figure 9, right panels) revealed the presence of transverse large-scale structures, organised in pairs with a streamwise length of about $\pi\delta$. The wavelength of these peaks corresponds to $n = L_\theta/\lambda_\theta = 3$ pairs of eddies at $Re_b = 4000$ and $n = L_\theta/\lambda_\theta = 2$ pairs at 20000 and 87000. Hence, we interpret the energy peaks in the streamwise spectra as the signature of cross-flow structures. Moreover, the spanwise size

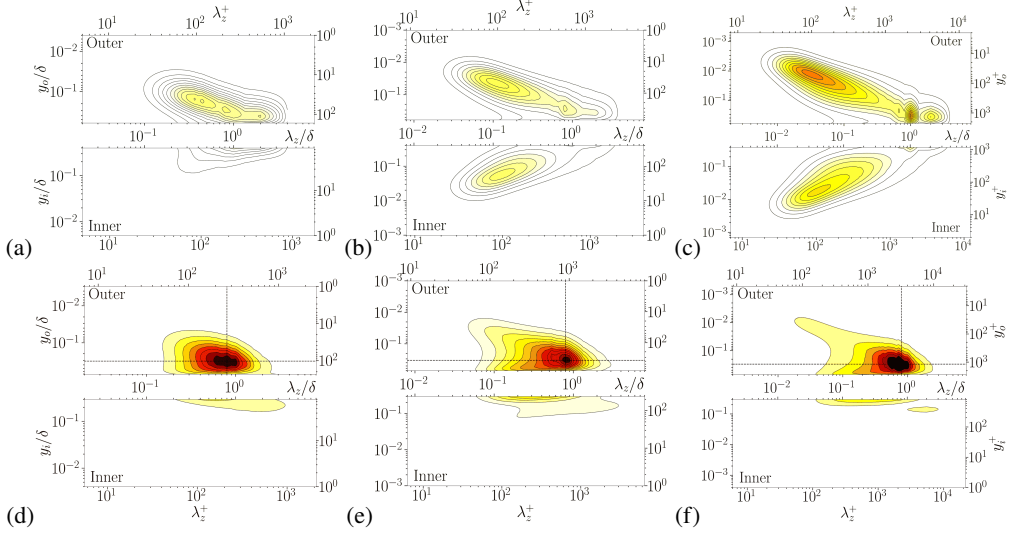


Figure 12: Pre-multiplied spectra of fluctuating wall-normal velocity ($k_z^* E_{vv}^*$) as a function of the spanwise wavelength and wall distance for the R40 flow cases (upper panels) and R1 flow cases (lower panels). From left to right, the panels correspond to $Re_b = 4000$ (a, d), 20000 (b, e), 87000 (c, f). Wall distance from the inner and outer wall and spanwise wavelength are reported in outer units (y_i/δ , y_o/δ , λ_z/δ) and local wall units (y_i^+ , y_o^+ , λ_z^+), respectively. Dashed lines mark the wavelength and wall-distance of the energy peak related to longitudinal large-scale structures.

of these structures is comparable with δ , thus we can ascribe to them also the peaks in the spanwise spectra at $\lambda_z/\delta \approx 2$.

In figure 12 we show the pre-multiplied spectral densities of wall-normal velocity fluctuations in the spanwise direction ($k_z^* E_{vv}^*$). In the R40 flow cases (upper panels) energy peaks related to near-wall turbulent structures form at $y_i^+ \approx y_o^+ \approx 50$, $\lambda_z^+ \approx 100$, except for the inner wall at $Re_b = 4000$, in agreement with the flow visualisations. Two secondary peaks in the channel core, more prominent at $Re_b = 87000$, highlight the presence of energetic modes with $\lambda_z/\delta \approx 1$ and $\lambda_z/\delta \approx 2$ at $y_o/\delta \approx 0.3$. Following the same reasoning about the streamwise velocity spectra, we trace these energetic modes to longitudinal roll cells, which generate large-scale radial sweeps and ejections. The effect of strong curvature on the energy distribution of the wall-normal velocity fluctuations (lower panels) is rather striking. Contrary to streamwise velocity spectra, the energy content is now much higher in the case of strong curvature, which points to substantial structural changes. No distinct peak is observed in the inner part of the channel, which conveys that the transverse large-scale structures that we noted above have no impact (on average) on the wall-normal velocity fluctuations. A prominent energy peak is located at $y_o/\delta \approx 0.3$, $\lambda_z/\delta \approx 0.8$, marked by the intersection of the dashed lines. This energetic mode is not present in plane channel flow (see e.g. Cho *et al.* 2018) and cannot be related to cross-flow structures, which are more intense near the inner wall. Hence, we interpret them as the signatures of longitudinal roll cells. This would mean that the typical configuration of longitudinal large-scale structures consists of $n = L_z/\lambda_z = 10$ pairs of roll cells (with $L_z = 8$, $\lambda_z/\delta = 0.8$), which we will ascertain in the following.

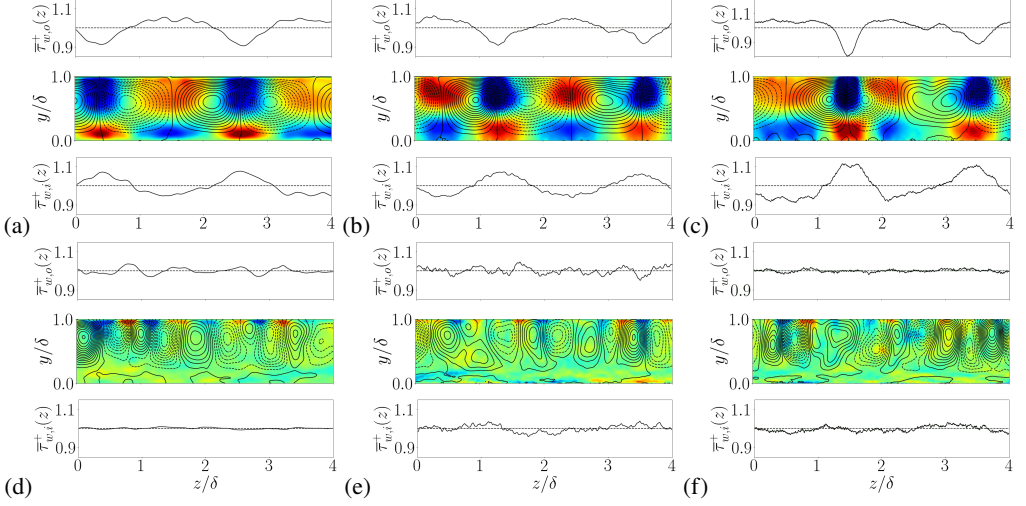


Figure 13: Coherent Stokes streamfunction ($\bar{\psi}$) in an (r, z) -plane overlaid to flooded contours of coherent streamwise velocity (\bar{u}^*), for the R40 flow cases (upper panels) and for the R1 flow cases (lower panels). From left to right, the panels correspond to $Re_b = 4000$ (a, d), 20000 (b, e), 87000 (c, f). Positive values of $\bar{\psi}$ (solid lines) indicate a clockwise-rotating roll cell, and vice-versa for negative values (dashed lines). The flooded contours range from -1.5 (blue) to 1.5 (red). Each panel shows the spanwise distribution of the mean shear stress at the two walls, $\bar{\tau}_{w,i}^+(z)$ and $\bar{\tau}_{w,o}^+(z)$, defined in (3.9). Only half of the domain is shown for the R1 flow cases.

3.4. Longitudinal large-scale structures

Flow visualisations and energy spectra reveal the presence of longitudinal large-scale structures, which are akin to the Dean vortices observed in laminar flow (Dean 1928). To understand how these structures depend on curvature and Reynolds number and how they affect the flow field, we separate the coherent contribution from the underlying turbulence, where coherence is intended in the sense given by Hussain (1986). For that purpose we use the triple decomposition of Hussain & Reynolds (1970), whereby a generic field variable, $\varphi(\theta, r, z, t)$, is decomposed as

$$\varphi(\theta, r, z, t) = \Phi(r) + \tilde{\varphi}(r, z, t) + \varphi''(\theta, r, z, t), \quad (3.6)$$

where Φ is the space average over the homogeneous directions (θ, z) and time (t) ,

$$\tilde{\varphi}(r, z, t) = \langle \varphi(\theta, r, z, t) \rangle_\theta - \Phi(r), \quad (3.7)$$

is the coherent contribution from the longitudinal vortices, $\langle \varphi(\theta, r, z, t) \rangle_\theta$ is the average over the streamwise direction, and

$$\varphi''(\theta, r, z, t) = \varphi(\theta, r, z, t) - \langle \varphi(\theta, r, z, t) \rangle_\theta \quad (3.8)$$

is the instantaneous turbulent fluctuation. The total fluctuation is then $\varphi' = \tilde{\varphi} + \varphi''$. The instantaneous coherent fields ($\tilde{\varphi}$) are averaged over time to obtain the mean coherent contribution ($\bar{\tilde{\varphi}}$). Since the time average is taken over a finite window, it is impossible to determine whether the longitudinal vortices are moving on a timescale longer than the averaging window. If they are slowly drifting, the time averages would underestimate their strength (Moser & Moin 1987). The results of the eduction procedure are presented in figure 13, where we show the mean coherent Stokes streamfunction ($\bar{\psi}$), defined such that $\bar{w} = \partial \bar{\psi} / \partial r$, $\bar{v} = -\partial \bar{\psi} / \partial z$. The overlaid flooded contours represent the mean coherent

streamwise velocity (\bar{u}^*). In addition, we report the spanwise distribution of the mean shear at the inner and outer wall,

$$\tau_{w,i}^+(z) = \frac{\nu}{u_{\tau,i}^2} \frac{\partial \langle u \rangle_{\theta,t}}{\partial r} \Big|_{r_i}, \quad \tau_{w,o}^+(z) = \frac{\nu}{u_{\tau,o}^2} \frac{\partial \langle u \rangle_{\theta,t}}{\partial r} \Big|_{r_o}. \quad (3.9)$$

In the R40 flow cases (upper panels) two pairs of counter-rotating vortices appear which nearly span the whole channel thickness and with a spanwise wavelength $\lambda_z/\delta \approx 2$, which is in agreement with the energy spectra in figure 10. Longitudinal roll cells with the same size were detected by Moser & Moin (1987). The spanwise inhomogeneity due to these secondary eddies has a strong impact on the wall shear. Indeed, large-scale ejections are generated between any pair of counter-rotating vortices (blue contours), where low-speed fluid is diverted away from the wall, and local friction attains a minimum. Correspondingly, large-scale sweeps generate at the opposite wall whereby high-speed fluids is pushed towards the wall (red contours), causing local increase of wall friction. This tendency is clearer as the Reynolds number increases, as one can infer from the spanwise distribution of the local wall shear, which shows excursions of about 10% at $Re_b = 4000$ (a) and $Re_b = 20000$ (b), and reaching up to 20% at $Re_b = 87000$ (c).

As for the R1 flow cases (lower panels), the number of pairs of counter-rotating vortices increases to about ten (only five are visible as half of the domain is shown). Hence, the spanwise wavelength of the roll cells is $\lambda_z/\delta \approx 0.8$, which corresponds to what found from the spectral analysis in figure 12. Spanwise shortening of the longitudinal roll cells is also observed in rotating channel flows, in which similar vortices develop on account of Coriolis forces (Matsson & Alfredsson 1990). Through DNS of rotating channel flow, Brethouwer (2017) found that the size of the longitudinal roll cells is smaller at higher rotation numbers (the rotation number in rotating channel flow is the counterpart of the curvature ratio in curved channels), in agreement with previous numerical studies (Kristoffersen & Andersson 1993; Yang & Wu 2012). In addition, Brethouwer (2017) found that the size of the roll cells is independent of the Reynolds number, which is also the case here. In fact, due to strong channel curvature, the roll cells are pushed towards the outer wall and cannot fill the entire channel height. Hence, the flow region near the inner wall (say, $y/\delta < 0.2$) is not affected, as seen in the spanwise distribution of the wall shear, which is nearly flat. As for the shear at the outer wall, spanwise excursions of $\tau_{w,o}^+(z)$ have a maximum amplitude of about 4% at $Re_b = 4000$ (d) and $Re_b = 20000$ (e), whereas they are very small at $Re_b = 87000$ (f), at which the effect of the longitudinal vortices is outweighed by turbulence. The reason why the outer-wall shear is barely affected by longitudinal vortices is their unsteadiness. The coherent streamfunction shows indeed that roll cells are less organised in the R1 flow cases than in R40, and on average they do not affect the streamwise velocity. Nonetheless, the impact of those eddies on the instantaneous flow is certainly not negligible in the case of strong curvature. The strength of longitudinal large-scale structures can be quantified in terms of the maximum amplitude of the coherent wall-normal velocity (Canton *et al.* 2016), which results in $\max|\tilde{v}|/u_b \approx 6\%$ for the R40 flow cases, nearly independent of the Reynolds number. Longitudinal vortices in the R1 flow cases are much stronger, their strength being $\max|\tilde{v}|/u_b \approx 20\%$ at $Re_b = 4000$, 14% at $Re_b = 20000$, 12% at $Re_b = 87000$.

3.5. Splitting and merging events

The eduction procedure based on triple decomposition allowed to quantify the mean configuration of longitudinal large-scale structures. However, the energy spectra highlighted the presence of multiple energy peaks at large wavelengths, which are particularly evident for the R40 flow case at $Re_b = 87000$ (figure 10). Multiple peaks suggest either the coexistence

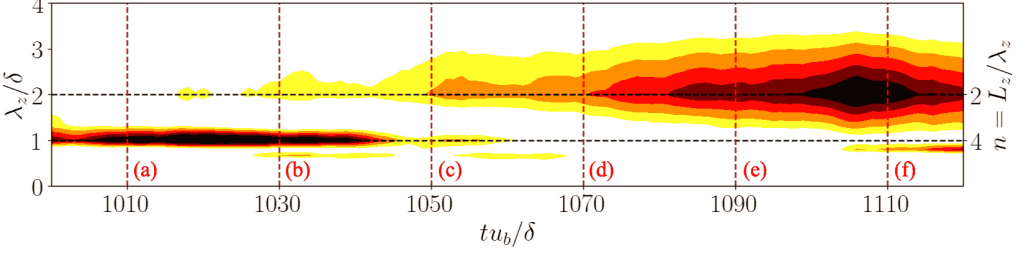


Figure 14: Time history of the pre-multiplied spanwise energy spectra of fluctuating streamwise velocity ($k_z^* E_{uu}^*$) for the R40 flow case at $Re_b = 87000$, fixed the wall distance at $y/\delta = 0.8$. The black dashed lines correspond to $\lambda_z/\delta = 2$ and $\lambda_z/\delta = 1$, at which the expected number of longitudinal vortices are indicated on the right vertical axis.

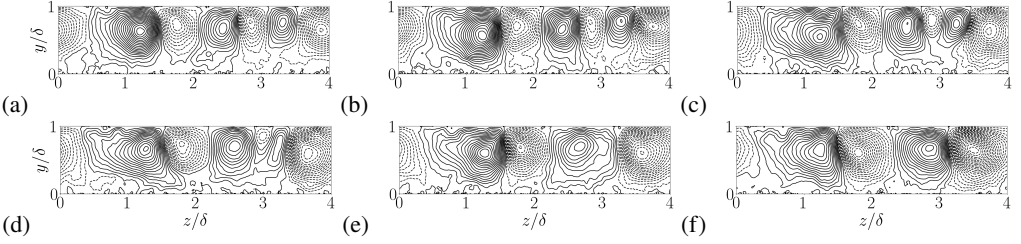


Figure 15: Coherent streamfunction ($\tilde{\psi}$) at the time instants marked by the red dashed lines in figure 14, for the R40 flow case at $Re_b = 87000$.

of large-scale structures of different sizes, or the occurrence of splitting and merging events. To clarify this point, we inspect the time history of the spanwise energy spectra of streamwise velocity fluctuations, shown in figure 14 for the R40 flow case at $Re_b = 87000$, at the wall distance where the peak of the energy associated with the longitudinal vortices occurs. A time window from $tu_b/\delta = 1000$ to 1120 was selected for the analysis and we took six subsequent snapshots of $\tilde{\psi}$, shown in figure 15, at intervals of $20\delta/u_b$ marked by the red dashed lines in figure 14. From $tu_b/\delta \approx 1000$ to 1040 most energy is clustered around $\lambda_z/\delta = 1$, hence $n = 4$ pairs of vortices would be expected (the number of vortices pairs is indicated on the right vertical axis). However, the snapshots of $\tilde{\psi}$ at $tu_b/\delta \approx 1010$ (a) and 1030 (b) reveal the occurrence of $n = 3$ pairs. In this respect, we note that the roll cells are not uniform in size, as the pair centred at $z/\delta \approx 0.5$ has a wavelength $\lambda_z/\delta \approx 2$, whereas the two remaining pairs have a wavelength $\lambda_z/\delta \approx 1$. A possible explanation is that the two pairs of small-size vortices are stronger than the large-size one, hence more energy is concentrated at $\lambda_z/\delta = 1$. A vortex-merging event is observed between $tu_b/\delta \approx 1050$ and 1090 . Panels (c) and (d) depict that the pair of smallest vortices located at $z/\delta \approx 3$ decrease in size and strength, as the iso-lines of the streamfunction get sparser. This process continues until the smallest pair is embedded within the adjacent clockwise rotating vortex (e), which appears more regular and strong at $tu_b/\delta \approx 1110$ (f). From $tu_b/\delta \approx 1080$ on, the energy peak is clustered around $\lambda_z/\delta = 2$ and, as expected, $n = 2$ pairs of roll cells are found.

The results obtained for the R1 flow case at $Re_b = 87000$ are presented in figure 16, which reports the time evolution of the spanwise spectra of the wall-normal velocity at the peak position of energy associated with the longitudinal vortices. The time window under scrutiny is half as for the R40 flow case, and the six subsequent snapshots of $\tilde{\psi}$, shown in figure 17, are sampled at intervals of $10\delta/u_b$ instead of 20 on account of stronger unsteadiness in cases with strong curvature. The time evolution of the spectra shows that the energy peak is

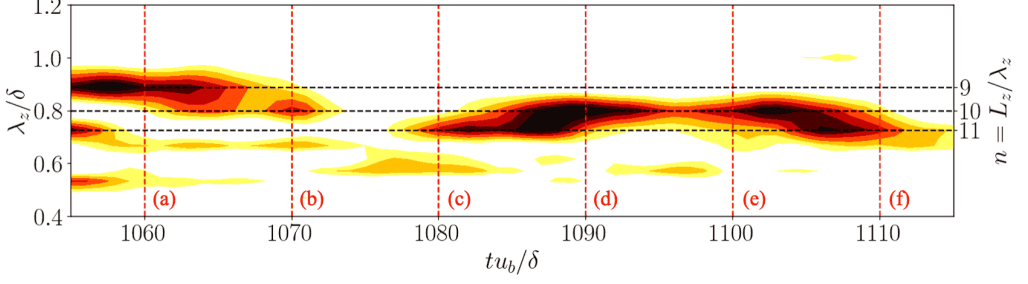


Figure 16: Time history of the pre-multiplied spanwise energy spectra of fluctuating wall-normal velocity ($k_z^* E_{vv}^*$) for the R1 flow case at $Re_b = 87000$, fixed the wall distance at $y/\delta = 0.7$. The black dashed lines correspond to $\lambda_z/\delta = 0.73$, $\lambda_z/\delta = 0.8$ and $\lambda_z/\delta = 0.89$, at which the expected number of longitudinal vortices are indicated on the right vertical axis.

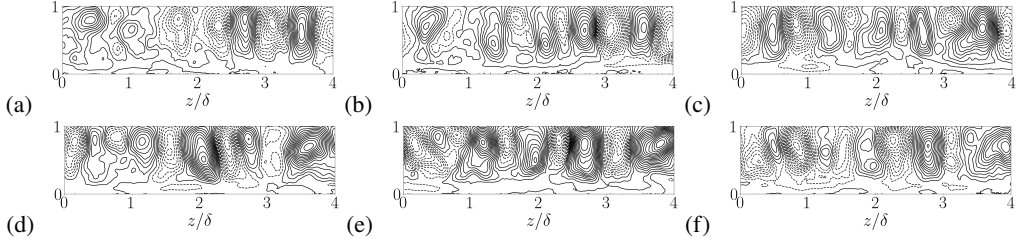


Figure 17: Coherent streamfunction ($\tilde{\psi}$) at the time instants marked by the red dashed lines in figure 16 for the R1 flow case at $Re_b = 87000$. Only half of the domain is shown.

clustered around $\lambda_z/\delta \approx 0.89$ from $tu_b/\delta = 1055$ to 1065 . Consistently, figure 17(a) displays nine vortices in the region under scrutiny ($n = 9$ pairs are present in the whole domain). This configuration seems to be unstable because of the ill-defined structure of the vortices pair located at $z/\delta \approx 1$, and because two counterclockwise vortices are adjacent straddling $z/\delta \approx 2$. At $tu_b/\delta = 1070$ the energy peak shifts at $\lambda_z/\delta \approx 0.8$, indeed the related figure 17(b) shows that a new clockwise rotating vortex emerged at $z/\delta \approx 2.2$ fitting in between the two counterclockwise rotating vortices and increasing the number of vortices to 10 (i.e. $n = 10$). The number of vortex pairs increase further to $n = 11$ at $tu_b/\delta \approx 1080$, as visible in figure 17(c), and the energy peak decreases accordingly to $\lambda_z/\delta \approx 0.73$. From $tu_b/\delta \approx 1085$ to 1105 the energy peak settles at $\lambda_z/\delta \approx 0.8$, and panels (d) and (e) highlight that the vortex configuration consists of $n = 10$ pairs. The energy peak shifts again to $\lambda_z/\delta \approx 0.73$ at $tu_b/\delta = 1110$. Figure 17(f) shows that the main vortexes are still ten, however small secondary vortices tend to split off from the primary ones, bringing more energy to smaller scales. In the case of strong curvature, the transitions from one vortex configuration to the other can be attributed to the unsteady dynamics of the vortices, which can be inferred from their spanwise motions, distorted shapes and different sizes, rather than to splitting and merging phenomena, which could not be clearly identified.

3.6. Role of longitudinal vortices on velocity fluctuations

In figure 18 we show the root-mean-square (RMS) of the streamwise (a, b) and wall-normal (c, d) velocity fluctuations, as well as the turbulent shear stress (e, f). Total fluctuations are reported along with the contributions due to the longitudinal vortices, which we have determined by taking the root-mean-square of the coherent contribution (3.7) along the spanwise direction and in time. For the R40 flow cases, the streamwise velocity fluctuations (a)

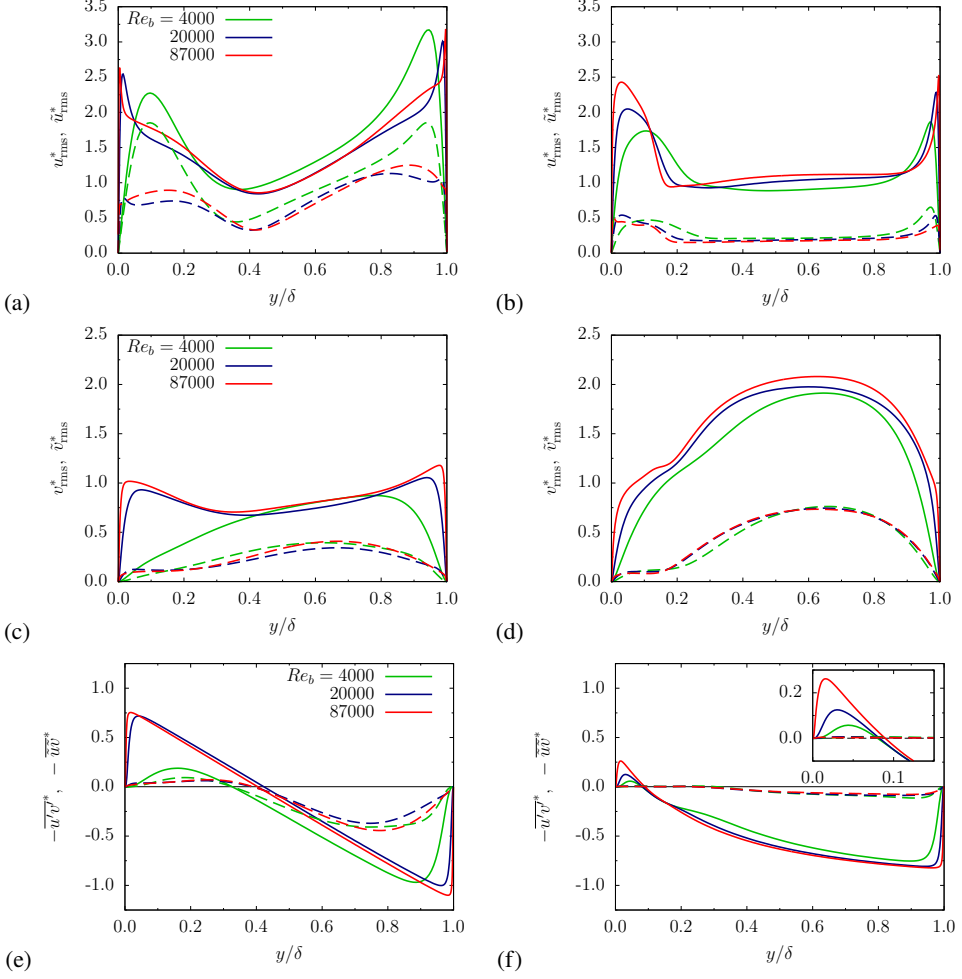


Figure 18: Profiles of root-mean-square streamwise (a, b) and wall-normal (c, d) velocity fluctuations and mean turbulent shear stress (e, f) at various Reynolds numbers for the R40 flow cases (left panels) and R1 flow cases (right panels). Solid lines refer to total fluctuations and dashed lines refer to coherent fluctuations due to longitudinal vortices.

are higher at the outer than at the inner wall. As made clear from the increased intensity of the coherent fluctuations, this asymmetry is mainly due to the longitudinal vortices, which are stronger near the outer wall. An exception is the case at $Re_b = 4000$ (green line), in which the coherent contribution at the outer wall is comparable to that on the inner wall. In general, the coherent contribution is about half of the total. The peak of the coherent contribution occurs between $y/\delta \approx 0.8$ and $y/\delta \approx 0.9$, corresponding to a bump in the profile of the total fluctuations. As for the R1 flow cases, the profiles of streamwise velocity fluctuations (b) show a near-wall peak on the concave side comparable to that of the corresponding R40 flow cases, and little contribution from coherent fluctuations. The profile of the velocity fluctuations is almost flat in the channel core, and the near-wall peak on the convex side is very different from the case with mild curvature, extending much farther from the wall. Wall-normal velocity fluctuations are only relevant in the channel core, with a peak at $y/\delta \approx 0.7$. For the R1 flow cases (d) fluctuations of wall-normal velocity are up to two times larger than

the streamwise velocity. Substantial contribution is found to be provided by the coherent fluctuations, which also attain a peak at $y/\delta \approx 0.7$, as observed in the velocity spectra.

As for the turbulent shear stress, it is nearly symmetrical in fully-turbulent R40 flow cases (e), resembling the case of a plane channel (see e.g. Kim *et al.* 1987). However, two differences should be noted: 1) the point of zero crossing is shifted towards the inner wall, at $y/\delta \approx 0.4$, and 2) the peak value increases near the outer wall and decreases near the inner wall. The effect of convex curvature is particularly evident at $Re_b = 4000$, at which the zero crossing is even closer to the inner wall. The coherent turbulent stress is about half of the total at $y/\delta \approx 0.8$, pointing to significant contribution of longitudinal vortices to momentum transport. Similar conclusions were also reached by Moser & Moin (1987) and Brethouwer (2022). The effects of strong curvature are substantial, as shown in panel (f). In the channel core, where viscous effects are negligible, the turbulent stress profile is no longer linear but rather quadratic, as after the analytical distribution of the total shear stress (C 2). As seen in the inset of the panel (f), the peak value is greatly reduced near the inner wall, which is in accordance with the findings reported by So & Mellor (1973) from experiments on turbulent boundary layers over a convex surface. The reason of the Reynolds stress reduction near the inner wall will be investigated in the following. The coherent shear stress becomes very small near the inner wall, since the longitudinal vortices are pushed towards the outer wall, as explained in §3.4.

3.7. Transverse large-scale structures

Visualisations of the flow near the inner wall of strongly curved channels (figure 9) revealed the presence of alternating regions of positive/negative velocity fluctuations elongated along the spanwise direction. Those wavy patterns are the footprint of transverse large-scale structures, which are originated from streamwise instabilities (Finlay *et al.* 1988) and which are convected at the mean flow speed (Matsson & Alfredsson 1992). As we did for the longitudinal vortices, we exploit triple decomposition to separate the effects of the cross-stream structures from those of turbulence. A field variable, $\varphi(\theta, r, z, t)$, is decomposed as

$$\varphi(\theta, r, z, t) = \Phi(r) + \hat{\varphi}(\theta, r, t) + \varphi'''(\theta, r, z, t) \quad (3.10)$$

where

$$\hat{\varphi}(\theta - tu_c/r, r, t) = \langle \varphi(\theta, r, z, t) \rangle_z - \Phi(r) \quad (3.11)$$

is the contribution of the transverse structures, $\langle \varphi(\theta, r, z, t) \rangle_z$ is the average along the spanwise direction, and $\varphi'''(\theta, r, z, t)$ is the instantaneous turbulent fluctuation. Since the transverse structures are advected with the flow, phase alignment is required to educe the associated coherent contribution. The time averages are evaluated by shifting each subsequent z -averaged field by an angle $\Delta\theta = \Delta tu_c/r_c$ where $\Delta t = \delta/u_b$ is the inverse of the sampling rate, u_c is the convection velocity and r_c is the curvature radius. The convection velocity was preliminarily estimated as the speed needed to retain maximum coherence in time, which resulted in $u_c \approx 0.67u_b$. This result was corroborated from the analysis of the wavenumber-frequency spectra of the streamwise velocity fluctuations for the R1 flow case at $Re_b = 4000$ (further details are given in the appendix D). When scaled by the friction velocity at the inner wall, the convection velocity at $Re_b = 4000$ is $u_c^+ \approx 11$, which is comparable with the convection velocity of the near-wall energy-containing eddies (Kim & Hussain 1993; Jimenez *et al.* 2001).

In figure 19 we show the mean coherent Stokes streamfunction ($\overline{\hat{\psi}}$), defined such that $\hat{v} = (\partial \hat{\psi} / \partial \theta) / r$, $\hat{u} = -\partial \hat{\psi} / \partial r$, overlaid to flooded contours of the mean coherent pressure ($\overline{\hat{p}^*}$) in a (θ, r) -plane. Alternating high- and low-pressure regions are observed, marking the

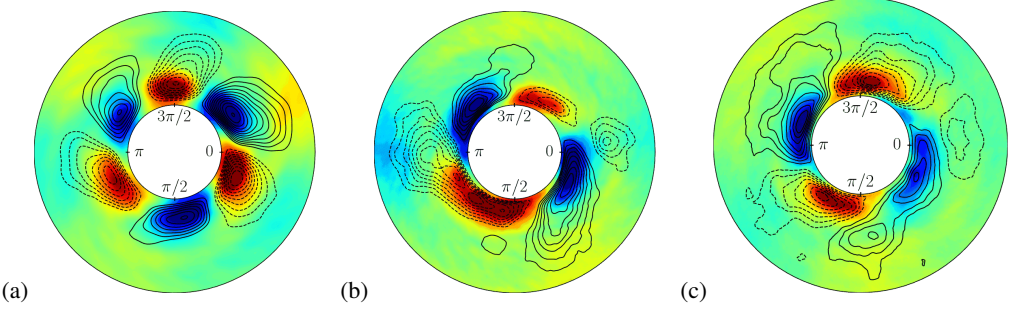


Figure 19: Mean coherent Stokes streamfunction ($\bar{\psi}$) overlaid to flooded contours of the mean coherent pressure (\bar{p}^*) in a (θ, r) -plane for the R1 flow cases at $Re_b = 4000$ (a), 20000 (b), 87000 (c). Positive values of $\bar{\psi}$ (solid lines), indicate a clockwise-rotating roll cell, associated with negative coherent pressure (blue contours), whereas negative (dashed lines) correspond to counter-clockwise rolls and positive coherent pressure (red contours). The mean flow is clockwise.

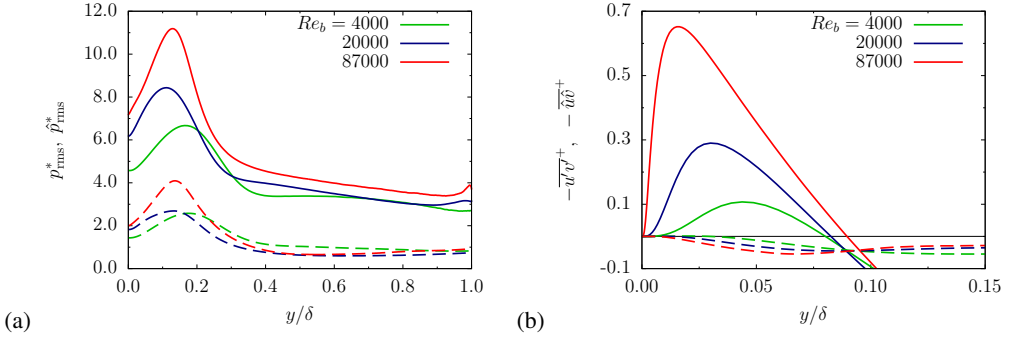


Figure 20: Profiles of RMS pressure fluctuations (a) and mean turbulent stress near the inner wall (b) at various Reynolds numbers, for the R1 flow cases. Solid lines refer to total fluctuations and dashed lines refer to coherent fluctuations due to transverse large-scale structures (the latter are denoted with ‘hat’).

presence of the transverse large-scale structures. Those are organised into three pairs of roll cells at $Re_b = 4000$ (a), whereas only two pairs are found at $Re_b = 20000$ (b) and 87000 (c). This result is in agreement with our interpretation of the streamwise energy spectra (figure 11). Although the radial extension of the transverse structures is comparable with δ , they are most intense near the inner wall and weaker towards the outer wall. The streamfunction shows that the cross-stream structures have an irregular shape and tend to split at high Reynolds number. This more chaotic organisation yields reduced strength of the transverse structures, which can be measured by the maximum amplitude of the coherent streamwise velocity, $\max|\hat{u}|$. Indeed, we found $\max|\hat{u}|/u_b \approx 9\%$ at $Re_b = 4000$ and $\max|\hat{u}|/u_b \approx 7\%$ at 20000 and 87000, hence transverse large-scale structures are about half as strong as longitudinal (see §3.4). The centres of the roll cells are approximately at the same location as the local minima of the mean shear rate (figure 5), supporting the idea that the transverse structures originate from a shear-layer instability (Finlay *et al.* 1988; Yu & Liu 1991).

Figure 20(a) displays the distributions of the RMS pressure fluctuations for the R1 flow cases, and includes the contribution of coherent fluctuations due to the transverse structures, which are obtained from the spanwise-coherent contribution as from equation (3.11). Near the inner wall, pressure fluctuations attain a peak which is twice as high as the outer-wall at

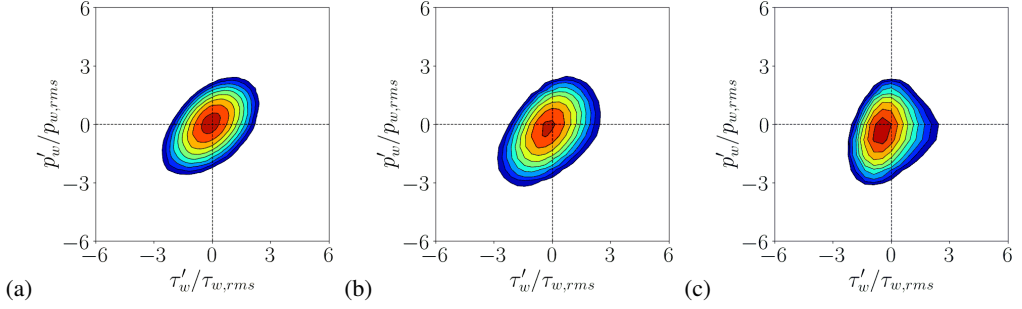


Figure 21: Joint PDF of wall shear and pressure fluctuations at the inner wall, $P(\tau'_w, p'_w)$, for the R1 flow cases at $Re_b = 4000$ (a), 20000 (b) and 87000 (c).

$Re_b = 4000$, and almost four times as high at $Re_b = 87000$. The impact of the transverse coherent structures on pressure fluctuations is substantial, as the peak value of the coherent contribution near the inner wall is about one third of the total. Another effect of spanwise structures, which is related to the increase of pressure fluctuations, is the suppression of the turbulent shear stress. This can be ascertained in figure 20(b), where we show the total turbulent stress (solid lines) and the coherent turbulent stress due to transverse structures (dashed lines). The results is that the coherent turbulent stress yields a negative contribution, meaning that the transverse structures tend to suppress ejections and sweeps near the inner wall. A similar result was reported by Kuwata (2022) simulating a turbulent flow over high-aspect-ratio longitudinal ribs, in which case the spanwise large-scale structures (originated by a Kelvin-Helmholtz instability) were found to increase locally pressure fluctuations and suppress the turbulent shear stress.

3.8. Role of transverse structures on wall shear and pressure

Suppression of the turbulent shear stress associated with spanwise-coherent structures was found to yield frictional drag reduction by many authors (Koumoutsakos 1999; Fukagata *et al.* 2005; Mamori & Fukagata 2011). In addition, experiments on turbulent boundary layers revealed that characteristic and identifiable variation of the wall pressure accompanies the advection of large organised structures, which are responsible for variation of the wall shear stress (Thomas & Bull 1983). To understand whether transverse large-scale structures play a role in drag reduction at the inner wall, we then investigate if strong pressure fluctuations due to the spanwise-coherent structures have an impact on friction at the inner wall. For that purpose, we preliminarily verify whether those quantities are correlated by inspecting the joint PDF of the wall shear stress and of the fluctuating pressure at the inner wall, $P(\tau'_w, p'_w)$, which we report in figure 21. Strong positive correlation emerges at $Re_b = 4000$ (a) and 20000 (b), at which flow near the inner wall is dominated by spanwise-coherent structures. This correlation becomes less distinct at 87000 (c), at which turbulent fluctuations start reach down to the near-wall region. Hence, the effect of spanwise-coherent structures at the inner wall is to enhance pressure fluctuations, which are strongly correlated with shear stress fluctuations.

Strong fluctuations of the wall shear can contribute to friction reduction at the inner wall by increasing the number of backflow events. This insight is supported by the PDF of the wall shear stress reported in figure 22. The mildly-curved cases, in which spanwise-coherent structures are not detected, can serve as a comparison. In addition, in table 2 we list the probability of backflow events. In the R40 flow cases (a) the PDFs of the inner-wall shear and of the outer-wall shear are nearly identical, with increasing probability of large values

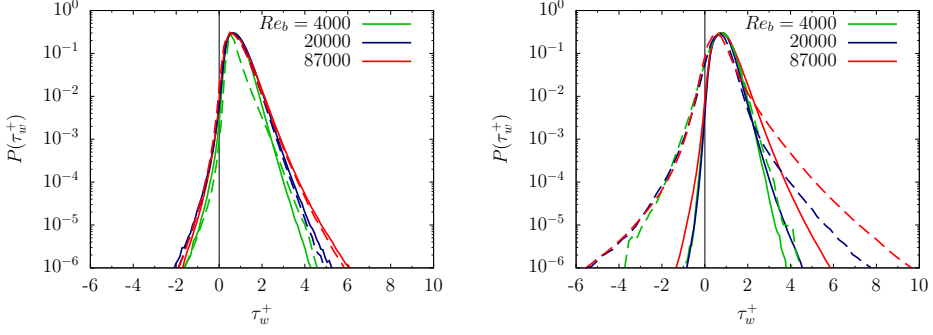


Figure 22: PDF of the wall shear stress, $P(\tau_w^+)$, at various Reynolds numbers for flow cases R40 (a) and R1 flow cases (b). Dashed lines refer to the inner wall and solid lines refer to the outer wall.

Re_b	r_c/δ	$P(\tau_{w,i}^+ < 0)$	$P(\tau_{w,o}^+ < 0)$
4000	40.5	0.05	0.08
20000	40.5	0.23	0.22
87000	40.5	0.36	0.22
4000	1.0	4.38	0.10
20000	1.0	3.92	0.09
87000	1.0	4.50	0.16

Table 2: Probability of backflow events at the two walls at various Reynolds numbers, for the R40 and R1 flow cases.

of positive shear as the Reynolds number increases. Backflow events are very rare, their probability not exceeding 0.3%. The picture is quite different for the R1 flow cases (b). As for the outer wall (solid lines), the probability of negative shear is even smaller than for the R40 flow cases. This results points to a possible analogy between the effect of favourable pressure gradient and concave curvature, since backflow probability decreases with flow acceleration (Zaripov *et al.* 2023). In contrast, the PDF tails widen at the inner wall (dashed lines), showcasing the enhancement of wall-shear fluctuations due to spanwise-coherent structures. The widening of the negative tail is associated with increase of the backflow events at the inner wall, whose probability exceeds 4%.

Further insights into the relationship between wall pressure and wall shear are provided in figure 23, where we show the streamwise distribution of the coherent pressure and of the coherent shear stress at the inner wall, both normalised by their maximum value. Streamwise inhomogeneity induced by spanwise-coherent structures imposes clear imprint on the wall pressure (blue lines), which features peaks and troughs corresponding to the high- and low-pressure regions observed in figure 19. The coherent wall shear stress (red lines) also features peaks and troughs, which we explain as follows. The coherent streamwise velocity of a clockwise-rotating roll cell (positive values of the streamfunction in figure 19) opposes the mean flow near the inner wall, reducing locally the streamwise velocity and hence the wall shear. Counter-clockwise rotating roll cells act in the opposite way. The small-scale oscillations of the wall-shear trend overlapping with the large-scale ones at $Re_b = 87000$ (c) are due to the presence of turbulent activity, which explains lower correlation between wall shear and wall pressure (see figure 21). The effects of spanwise-coherent structures on the

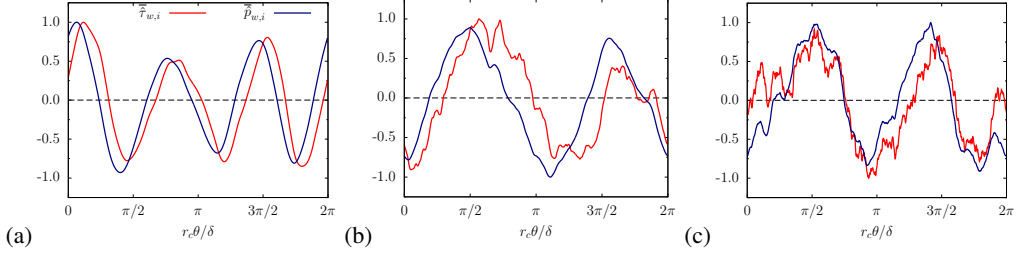


Figure 23: Streamwise distribution of mean coherent shear stress ($\bar{\tau}_{w,i}$, red lines), and mean coherent pressure ($\bar{p}_{w,i}$, blue lines) at the inner wall, for the R1 flow cases at $Re_b = 4000$ (a), 20000 (b), 87000 (c). Both quantities are normalised by their maximum value.

flow field can be further characterised by analysing the phase shift between the wall shear stress and the wall pressure. The wavy pressure distribution generates local pressure gradients in the streamwise direction, which tend to accelerate and decelerate the fluid and result in the alternating regions of high and low wall shear. Looking back at figure 19, one can see that high-pressure regions correspond to counter-clockwise rotating eddies, vice-versa for the low-pressure regions. Hence, between any pair of counter-rotating eddies where the flow is locally subjected to an adverse pressure gradient ($u' < 0$) high-speed fluid is pushed toward the inner wall ($v' < 0$). Between any neighbouring pair, there is a favourable pressure gradient ($u' > 0$) and simultaneously low-speed fluid is diverted away from the inner wall ($v' > 0$). In both cases, the combination of these motions yields to $-u'v' < 0$, explaining why spanwise structures make a negative contribution to the production of Reynolds shear stress, which we have highlighted in figure 20(b).

3.9. Quadrant analysis

To provide a quantitative basis for the qualitative analysis above, we consider the joint probability density function (JPDF) of streamwise and wall-normal fluctuations, $P(u', v')$, such that

$$-\overline{u'v'} = \int_{-\infty}^{+\infty} u'v'P(u', v')du'dv', \quad (3.12)$$

where the covariance integrand, $u'v'P(u', v')$, is a measure of the contribution of each pair of u' and v' to the turbulent shear stress (Wallace & Brodkey 1977). Each quadrant of the plane of the (u', v') plane corresponds to a class of motion, specifically Q2 and Q4 quadrant events correspond to ‘ejections’ ($u' < 0$ and $v' > 0$) and ‘sweeps’ ($u' > 0$ and $v' < 0$), yielding positive contribution to the turbulent shear stress, whereas Q1 and Q3 quadrants correspond to ‘outward interactions’ ($u' > 0$ and $v' > 0$), and ‘inward interactions’ ($u' < 0$ and $v' < 0$), which yield negative contribution to it.

In figures 24 and 25 we show flooded contours of $P(u', v')$ superimposed to iso-lines of $u'v'P(u', v')$, for the R40 and R1 flow cases, respectively. The joint PDF is evaluated in wall-parallel planes near the outer and the inner wall at $y^+ \approx 12$, which in plane channels is the ‘balance point’ where the contributions of ejections and sweeps are equal (Kim *et al.* 1987). In the R40 flow cases, the JPDF at the outer wall (upper panels) has a roughly elliptical shape with major axis inclined along the Q2 and Q4 quadrants, pointing to high probability of sweeps and ejections. Similar observations apply to the fully turbulent R40 flow cases near the inner wall (panels (e) and (f) of figure 24), and for the R1 flow cases near the outer wall (upper panels of figure 25). However, strong curvature seems to increase the

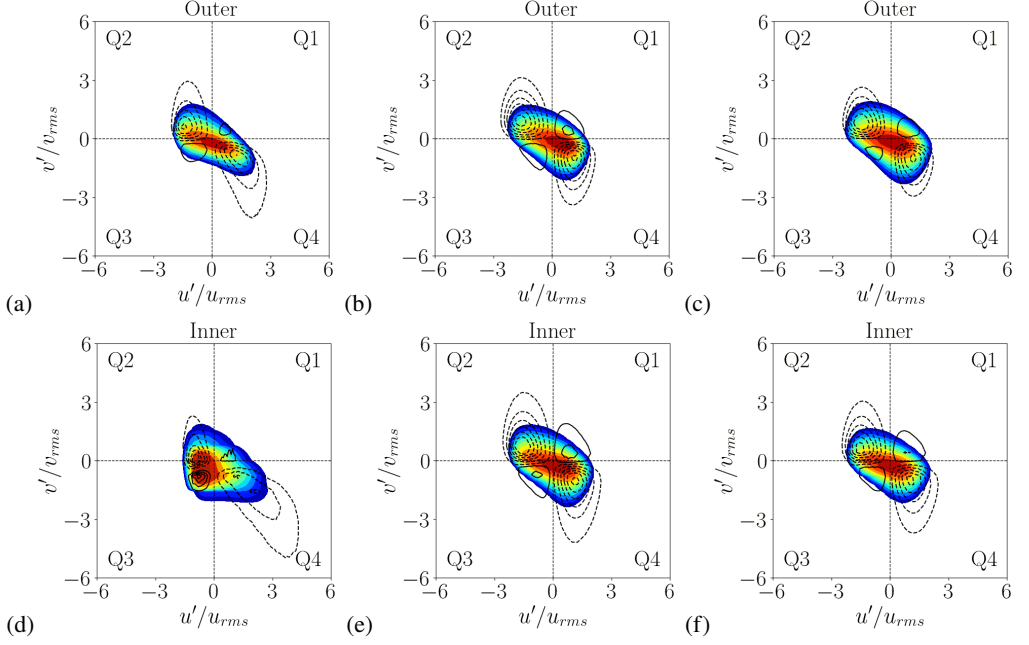


Figure 24: Joint PDF of streamwise and wall-normal velocity fluctuations, superimposed to flooded contours of the covariance integrand, near the outer wall (upper panels) and the inner wall (lower panels) at $y^+ \approx 12$, for the R40 flow cases. From left to right, the panels correspond to $Re_b = 4000$ (a, d), 20000 (b, e), 87000 (c, f).

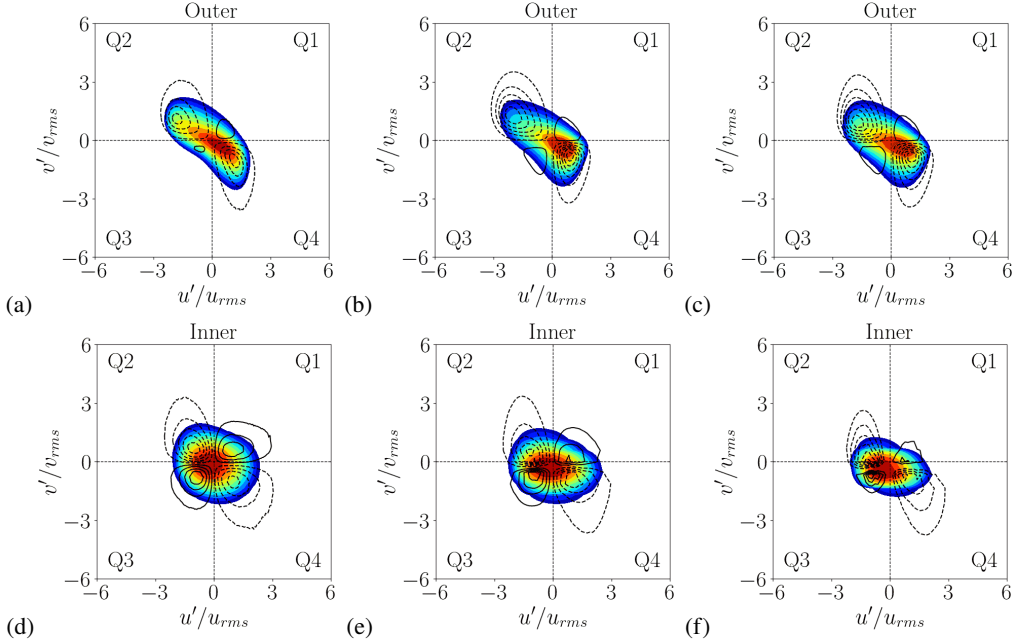


Figure 25: Joint PDF of streamwise and wall-normal velocity fluctuations, superimposed to flooded contours of the covariance integrand, near the outer wall (upper panels) and the inner wall (lower panels) at $y^+ \approx 12$, for the R1 flow cases. From left to right, the panels correspond to $Re_b = 4000$ (a, d), 20000 (b, e), 87000 (c, f).

Re_b	Q1	Q2	Q3	Q4
R40 outer wall				
4000	-8.90	+47.56	-7.90	+69.24
20000	-12.67	+66.64	-10.10	+56.13
87000	-16.60	+66.59	-11.63	+61.64
R40 inner wall				
4000	-30.76	+31.38	-11.82	+111.19
20000	-14.10	+63.82	-9.57	+59.86
87000	-17.26	+63.75	-10.81	+64.33
R1 outer wall				
4000	-5.09	+56.27	-2.43	+51.29
20000	-7.01	+72.47	-7.09	+41.64
87000	-9.58	+68.95	-9.51	+50.14
R1 inner wall				
4000	-75.25	+115.39	-65.18	+125.04
20000	-60.01	+95.88	-49.38	+113.52
87000	-39.40	+59.72	-21.18	+100.86

Table 3: Percentage contribution of quadrants to turbulent shear stress $(\overline{u'v'}_{Qi}/\overline{u'v'})$, for the R40 and R1 flow cases near the inner and outer wall, at $y^+ \approx 12$.

probability of sweeps more than ejections, which can be inferred from the shift of the JPDPF peak towards the Q4 quadrant. The scenario is different at the inner wall. In the R40 flow case at $Re_b = 4000$, depicted in figure 24(d), the peak probability is mainly concentrated in the Q2 and Q3 quadrants, and to a lesser extent in the Q4 quadrant, on account of higher and less probable values of u' and v' . The roughly circular shape of the JPDPF at the inner wall in the R1 flow cases (figure 25, lower panels) shows that the negative correlation between u' and v' , typical of the near-wall region of turbulent flows, vanishes. In addition, the covariance integrand highlights that the contribution to the turbulent stress is not dominated by the Q2 and Q4 motions, but strong contributions also come from the Q1 and Q3 motions.

More quantitative results are presented in table 3, where we list the integrated contributions to the turbulent shear stress from each quadrant $(\overline{u'v'}_{Qi}/\overline{u'v'})$, $i = 1, 2, 3, 4$ at $y^+ \approx 12$. For the R40 fully turbulent flow cases the results are comparable with experimental results for plane channel flow (Wallace *et al.* 1972), namely the contribution of both ejections and sweeps is about 70%, whereas inward and outward interactions each contribute negatively by about 20%. At $Re_b = 4000$, instead, the Q2 contribution near the inner wall reduces to 30%, which is comparable with the Q1 contribution but opposite in sign, whereas the Q4 contribution exceeds 110% of the shear stress. Comparing this value with the shape of the JPDPF in figure 24(d), one can infer that larger, energetic but infrequent motions are the main contributors to the turbulent shear stress. These strong sweeps can be attributed to the longitudinal vortices pushing the high-speed mean flow from the channel core towards the inner wall. As for the R1 flow cases, the quadrant contributions at the outer wall are similar to those of the R40 flow cases, except for greater contribution of ejections as compared to sweeps. Hence, the most probable motions (i.e. sweeps, as visible in figure 25) do not contribute as much to the turbulent shear stress as the ejections, see table 3. At the inner wall, the fractional contributions of the outward (Q1) and inward (Q3) interactions exceeds half the contributions of ejections (Q2) and sweeps (Q4). This result confirms that the transverse

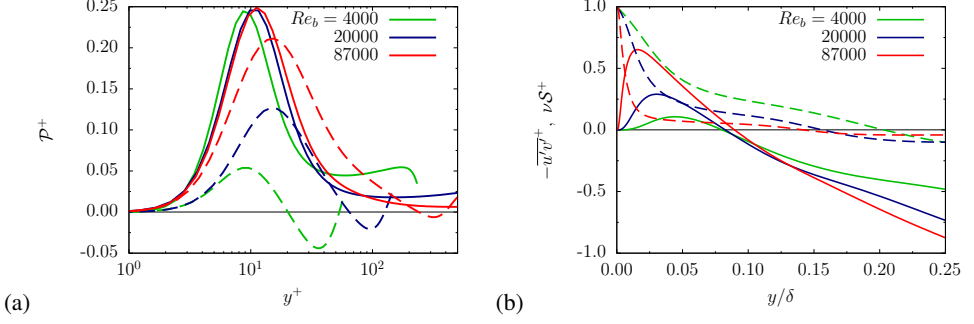


Figure 26: (a) TKE production (\mathcal{P}^+) near the outer wall (solid lines) and near the inner wall (dashed lines). (b) Turbulent shear stress ($-\overline{u'v'}^+$, solid lines) and viscous shear stress (νS^+ , dashed lines) near the inner wall. All quantities are reported in local wall units for the R1 flow cases.

large-scale structures, which were found to generate Q1 and Q3 motions in §3.8, play a key role in the strong attenuation of the turbulent shear stress near the inner wall of strongly curved channels.

3.10. Energy production reversal

Outward and inward interactions contribute negatively to turbulent shear stress, hence they yield negative contribution to the production of turbulence kinetic energy (TKE), $\mathcal{P} = -\overline{u'v'}S$, where $S = dU/dr - U/r$ is the mean shear rate. Based on the analysis in §3.9, we expect that TKE production be reduced near the inner wall in flow cases with strong curvature. In figure 26(a) we then show the TKE production for the R1 flow cases. Near the outer wall (solid lines) all curves tend to collapse, especially at high Reynolds number, revealing that the flow similarity is preserved near a concave surface. The peak production is located at $y^+ \approx 12$ (except at $Re_b = 4000$, for which the peak occurs at $y^+ \approx 9$) and the peak value is $\mathcal{P}^+ \approx 0.25$, similar to plane channel flow (Kim *et al.* 1987; Laadhari 2002). In contrast, TKE production near the inner wall (dashed lines) depends heavily on the Reynolds number, implying that classical wall scaling no longer holds near highly convex surfaces. Furthermore, a region where production is negative appears at each Reynolds number. For the production to be positive everywhere, the turbulent shear stress and the viscous shear stress must have the same sign and vanish at the same location. This is not the case for the strongly curved channel, as clearly illustrated in figure 26(b), which shows profiles of the turbulent shear stress, $-\overline{u'v'}^+$ (solid lines), and of the viscous shear stress, νS^+ (dashed lines), near the inner wall of the R1 flow cases. The displacement between the zero-crossings of the turbulent shear stress and of the viscous shear, the amplitude of which decreases slightly as the Reynolds number increases, is related to asymmetry of the mean velocity profile (Beguier *et al.* 2005) and leads to a region of opposing shear where $-\overline{u'v'}^+ < 0$ and $\nu S^+ > 0$, hence $\mathcal{P}^+ < 0$. As pointed out in §3.1, the point of vanishing shear marks the interface between the two distinct flow structures developing at each wall. Straddling this interface there is a diffusive transfer of shear stress from the outer- to the inner-wall region that has a sign opposite to the locally produced shear stress, leading to negative net TKE production (Hanjalić & Launder 1972). In the region with negative production a local energy reversal mechanism takes place, whereby energy is transferred from turbulent fluctuations to the mean flow (Eskinazi & Erian 1969). Besides its physical significance, this result provides useful caveat for use of RANS models for simulations of turbulent flows over convex walls.

In fact, standard eddy-viscosity models would clearly fail if turbulent shear stress and mean shear do not go to zero at the same location.

4. Conclusions

We have investigated fully developed flow in a curved channel to get insight into turbulence bounded by curved surfaces. This setup showcases rich physics due to the interplay of turbulence with large-scale coherent structures driven by centrifugal instabilities, which break the symmetry of the flow resulting in different behaviour near the convex and the concave walls. We have focused on the effects of curvature by examining two extreme cases, a mildly curved channel with radius of curvature $r_c/\delta = 40.5$ and a strongly curved channel with $r_c/\delta = 1$, where δ is the channel height. For each geometry, we have studied the effect of Reynolds number (Re_b) through an extensive series of DNS, covering flow regimes from laminar up to the moderately high value of $Re_b = u_b\delta/\nu = 87000$, where u_b is the bulk velocity and ν the kinematic viscosity. Our analysis has shown that the friction coefficient is somewhat higher as compared to the case of a plane channel. In addition, we have found that flow transition is anticipated by concave wall curvature and delayed by convex curvature, thus preventing turbulence to fully develop near the inner wall of strongly curved channels. Visualisations of the flow field have shown the presence of fine-scale turbulent structures as well as large-scale coherent structures elongated either in the streamwise and in the cross-stream directions. Through the spectral analysis of velocity fluctuations we detected the clear imprinting of the near-wall turbulence cycle at both walls in the case of mildly curved channels, whereas wall turbulence is virtually absent at the inner (convex) wall of strongly curved channels. Clear footprints of longitudinal and transverse large-scale structures were also found.

Longitudinal large-scale structures, originating from centrifugal instabilities and resembling the Dean vortices found in laminar flow, were identified through a vortex eduction based on triple decomposition, which allowed to quantify their effects on turbulence. Specifically, longitudinal coherent structures were found to depend weakly on Reynolds number and highly on the channel geometry. As channel curvature increases, vortices are displaced toward the outer wall, their size reduces and they become more unsteady. As a consequence, the mean spanwise distribution of the wall shear is modified by longitudinal vortices only in mildly curved cases. The effects of longitudinal coherent vortices on velocity fluctuations and turbulent shear stress were quantified, revealing that in mildly curved channels streamwise velocity fluctuations and momentum transport are greatly affected, whereas in strongly curved channels the wall-normal velocity component is the most influenced. Through the combined use of spectral analysis and triple decomposition, we have identified unsteady splitting and merging of the longitudinal coherent eddies. Transverse large-scale structures were found near the convex wall of strongly curved channels, whose footprint consists of pressure waves advected downstream at the mean flow speed. These structures were also characterised by using triple decomposition and phase averaging, showing that their effect is to enhance pressure fluctuations near the inner wall. This enhancement is correlated with increased fluctuations of the wall shear stress, which is responsible for friction reduction at the inner wall. The relationship between increased pressure fluctuations and decreased wall friction has been attributed to the generation of alternating favourable and adverse pressure gradients, which combine with upward and downward radial motions, respectively, suppressing the turbulent shear stress near the convex wall. This insight has been further explored and quantified through quadrant analysis of streamwise and wall-normal velocity fluctuations. An enhancement of inward and outward interactions has been found, leading

to the appearance of a region with negative production of turbulence kinetic energy in the strongly curved cases.

These results offer a valuable dataset for fundamental research on the interaction between turbulence and curved walls, as well as for turbulence modelling, e.g. subgrid-scale models for LES and RANS closures. We also believe that insights gained from the time-evolving curved channel flow may be relevant to boundary layers over both convex and concave surfaces. In fact, our analysis has shown that the interaction between the inner and outer wall regions is concentrated in the channel core, whereas the inner (outer) wall region is dominated by convex (concave) curvature effects. In this work, we focused on two values of curvature. Further investigation of additional curvatures is necessary to determine the critical value at which the coherence of near-wall streaks at the convex wall breaks down, and whether significant changes in flow physics occur with increasing curvature.

Acknowledgements. The results reported in this paper have been achieved using the EuroHPC Research Infrastructure resource LEONARDO based at CINECA, Casalecchio di Reno, Italy, under project EuroHPC 02044 and IskraB CONCORDE.

Funding. This research received financial support from ICSC-Centro Nazionale di Ricerca in ‘High Performance Computing, Big Data and Quantum Computing’, funded by European Union-NextGenerationEU.

Declaration of interests. The authors report no conflict of interest.

Data availability statement. All data that support the findings of this study are available from the corresponding author upon request.

Author ORCIDs.

G. Soldati, <https://orcid.org/0009-0007-4597-756X>;

P. Orlandi, <https://orcid.org/0000-0002-0305-5723>;

S. Pirozzoli, <https://orcid.org/0000-0002-7160-3023>.

Appendix A. Effects of domain size

Six additional simulations have been carried out to verify a-posteriori the adequacy of the domain sizes used in the DNS campaign. Here, we consider the Reynolds number $Re_b = 5000$, which is the least to have fully turbulent flow. As for the R40 flow cases, from the baseline configuration ($L_\theta/\delta = 2\pi$, $L_z/\delta = 4$) we have doubled and quadrupled both L_θ (for fixed L_z) and L_z (for fixed L_θ), by retaining the same grid spacing. As for the R1 flow cases, the streamwise extent of the domain resolves a full circumference, hence it was not increased. From $L_z/\delta = 8$ used in the baseline DNS, the spanwise extent was decreased by a factor two ($L_z/\delta = 4$) and increased by a factor two ($L_z/\delta = 16$). In figure 27 we show the mean streamwise velocity (a, b) and the RMS profiles of streamwise (green), wall-normal (blue) and spanwise (red) velocity fluctuations (c, d) for both the R40 flow cases (a, c) and R1 flow cases (b, d). One will see that all the profiles obtained with the different combinations of domain size (marked by the different line types) nearly collapse to a single line, showing that the domain size used in the DNS campaign is adequate.

Appendix B. Global friction velocity

The derivation of the global friction velocity has been shown by Brethouwer (2022) starting from the mean momentum balance, yet we believe that it may be instructive to illustrate briefly how it relates to the mean-pressure gradient. The analytical expression of the streamwise pressure gradient as a function of the shear stresses at the two walls can be derived in the simplest way from the balance of moments of forces about the centre of curvature, which,

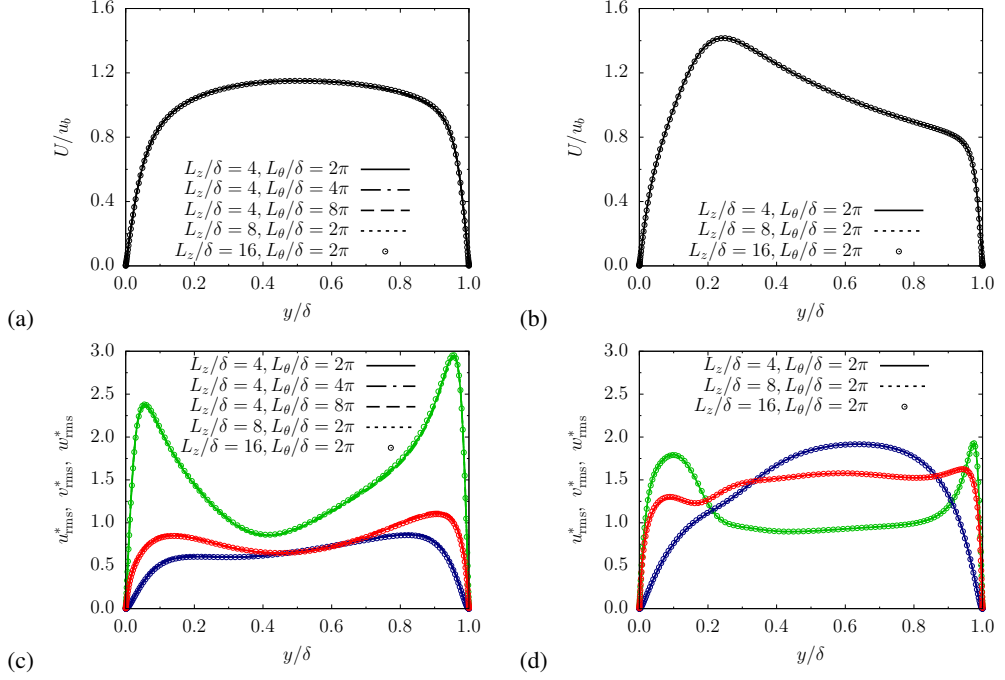


Figure 27: Mean streamwise velocity (U/u_b) for the R40 flow cases (a) and R1 flow cases (b); RMS profiles of streamwise (green), wall-normal (blue) and spanwise (red) velocity fluctuations for the R40 flow cases (c) and R1 flow cases (d). The Reynolds number is fixed at $Re_b = 5000$ and the domain size is varied as marked, case by case, by the different line types.

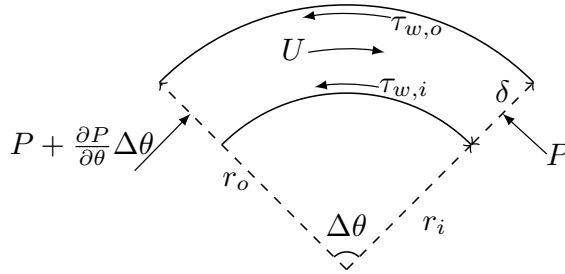


Figure 28: Sketch of the curved channel flow.

referring to the sketch of figure 28, reads

$$\int_{r_i}^{r_o} \left(-P - \frac{\partial P}{\partial \theta} \Delta\theta + P \right) r dr + \left(\tau_{w,i} r_i^2 + \tau_{w,o} r_o^2 \right) \Delta\theta = 0. \quad (\text{B } 1)$$

Hence, recalling that $r_c = (r_o + r_i)/2$ and $\delta = r_o - r_i$, we obtain

$$-\frac{dP}{d\theta} = \frac{\tau_{w,i} r_i^2 + \tau_{w,o} r_o^2}{r_c \delta}. \quad (\text{B } 2)$$

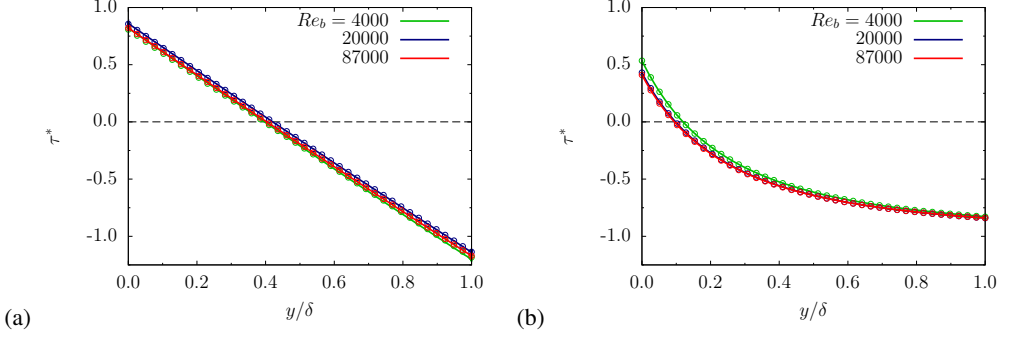


Figure 29: Mean profile of the total shear stress (τ^*) at various Reynolds numbers for the R40 flow cases (a) and R1 flow cases (b). Circles denote the analytical profile (C 2).

To define a global friction velocity, $u_{\tau,g}$, an equivalent length of the curved channel must be defined. Considering the length of the channel at the centreline, $L_\theta = r_c \Delta\theta$, one obtains

$$-\frac{1}{\rho r_c} \frac{dP}{d\theta} = 2 \frac{u_{\tau,g}^2}{\delta} \quad \Rightarrow \quad u_{\tau,g}^2 = \frac{u_{\tau,i}^2 r_i^2 + u_{\tau,o}^2 r_o^2}{2r_c^2} \quad (\text{B } 3)$$

where $u_{\tau,i}^2 = \tau_{w,i}/\rho$ and $u_{\tau,o}^2 = \tau_{w,o}/\rho$.

Appendix C. Convergence of flow statistics

Whether the statistics are well-converged can be verified by comparing the analytical profile of the total shear stress with the DNS results. As shown by Brethouwer (2022), starting from the mean momentum equation in streamwise direction for the curved channel flow, which reads

$$0 = -\frac{1}{\rho r} \frac{\partial P}{\partial \theta} + \nu \left(\frac{1}{r} \frac{\partial U}{\partial r} - \frac{U}{r^2} + \frac{\partial^2 U}{\partial r^2} \right) - \left(\frac{\partial \overline{uv}}{\partial r} + \frac{2}{r} \overline{uv} \right), \quad (\text{C } 1)$$

one can derive the following equation for the total shear stress distribution

$$\tau(r) = \frac{r_i^2 \tau_{w,i} (r_o^2 - r^2) + r_o^2 \tau_{w,o} (r_i^2 - r^2)}{2r^2 r_c \delta}. \quad (\text{C } 2)$$

In figure 29 we show the analytical profile of the total shear stress (circles) and the DNS results at the corresponding Reynolds numbers (solid lines). The DNS results effectively collapse to the analytical profile, which corroborates that satisfactory statistical convergence is achieved.

Appendix D. Estimation of the convection velocity

In figure 30(a) we show the wavenumber-frequency spectra of the streamwise velocity fluctuations, $E_{uu}^*(k_\theta, \omega)$, for the R1 flow case at $Re_b = 4000$. The wall distance is kept fixed at $y/\delta = 0.09$, which is the peak location of $k_\theta^* E_{uu}^*$ related to transverse structures (see figure 11). An energy peak appears in the spectral density at the wavenumber $k_\theta \delta \approx 3$ (marked by the vertical dashed line) corresponding to $\lambda_\theta/\delta \approx 2\pi/3$, which is the wavelength of transverse structures at $Re_b = 4000$ (see figure 11). As seen in figure 30(b), showing $E_{uu}^*(\omega)$ fixed the wavenumber at $k_\theta \delta = 3$, the energy peak is at the angular frequency $\omega \approx 2u_b/\delta$. Hence, the convection velocity of transverse structures can be estimated as $u_c = \omega/k_\theta \approx 0.67u_b$.

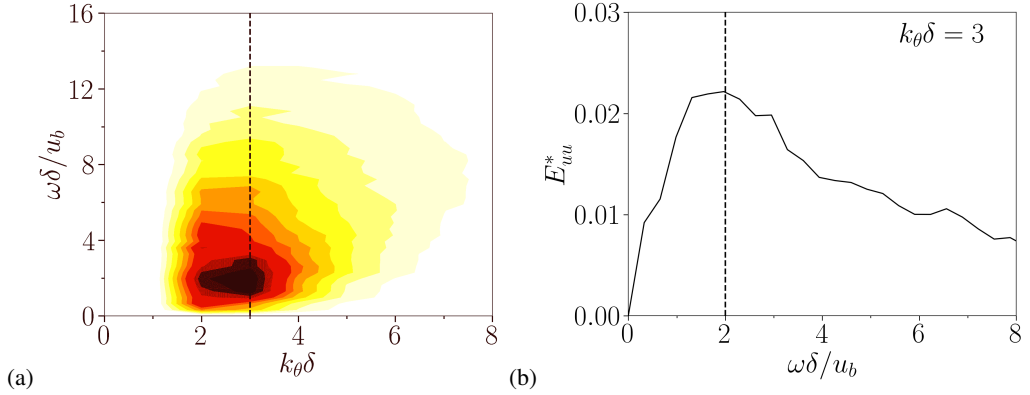


Figure 30: (a) Wavenumber-frequency spectra of the fluctuating streamwise velocity, $E_{uu}^*(k_\theta, \omega)$, for the R1 flow case at $Re_b = 4000$; (b) $E_{uu}^*(\omega)$ at $k_\theta \delta = 3$. The wall distance is fixed at $y/\delta = 0.09$.

REFERENCES

- ALFREDSSON, P. H. & PERSSON, H. 1989 Instabilities in channel flow with system rotation. *Journal of Fluid Mechanics* **202**, 543–557.
- BARLOW, R. S. & JOHNSTON, J. P. 1988 Structure of a turbulent boundary layer on a concave surface. *Journal of Fluid Mechanics* **191**, 137–176.
- BEGUIER, C., GIRALT, F., FULACHIER, L. & KEFFER, J. F. 2005 Negative production in turbulent shear flows. In *Structure and Mechanisms of Turbulence II: Proceedings of the Symposium on Turbulence Held at the Technische Universität Berlin, August 1–5, 1977*, pp. 22–35. Springer.
- BRADSHAW, P. & YOUNG, A. D. 1973 Effects of streamline curvature on turbulent flow. *Tech. Rep.* AG-169. Agard Paris.
- BRETHOUWER, G. 2017 Statistics and structure of spanwise rotating turbulent channel flow at moderate Reynolds numbers. *Journal of Fluid Mechanics* **828**, 424–458.
- BRETHOUWER, G. 2022 Turbulent flow in curved channels. *Journal of Fluid Mechanics* **931**, A21.
- BREWSTER, D. B., GROSBERG, P. & NISSAN, A. H. 1959 The stability of viscous flow between horizontal concentric cylinders. *Proceedings of the Royal Society of London. Series A. Mathematical and Physical Sciences* **251** (1264), 76–91.
- CANTON, J., ÖRLÜ, R., CHIN, C., HUTCHINS, N., MONTY, J. & SCHLATTER, P. 2016 On large-scale friction control in turbulent wall flow in low Reynolds number channels. *Flow, Turbulence and Combustion* **97**, 811–827.
- CHO, M., HWANG, Y. & CHOI, H. 2018 Scale interactions and spectral energy transfer in turbulent channel flow. *Journal of Fluid Mechanics* **854**, 474–504.
- DAI, Y. J., HUANG, W. X. & XU, C. X. 2016 Effects of Taylor-Görtler vortices on turbulent flows in a spanwise-rotating channel. *Physics of Fluids* **28** (11).
- DEAN, W. R. 1928 Fluid motion in a curved channel. *Proceedings of the Royal Society of London. Series A, Containing Papers of a Mathematical and Physical Character* **121** (787), 402–420.
- ECKHAUS, W. 1965 Studies in non-linear stability theory.
- ELLIS, L. B. & JOUBERT, P. N. 1974 Turbulent shear flow in a curved duct. *Journal of Fluid Mechanics* **62** (1), 65–84.
- ESKINAZI, S. & ERIAN, F. F. 1969 Energy reversal in turbulent flows. *Physics of Fluids* **12** (10), 1988–1998.
- ESKINAZI, S. & YEH, H. 1956 An investigation on fully developed turbulent flows in a curved channel. *Journal of the Aeronautical Sciences* **23** (1), 23–34.
- FINLAY, W. H., KELLER, J. B. & FERZIGER, J. H. 1988 Instability and transition in curved channel flow. *Journal of Fluid Mechanics* **194**, 417–456.
- FUKAGATA, K., KASAGI, N. & SUGIYAMA, K. 2005 Feedback control achieving sublamina friction drag. In *Proceedings of the 6th Symposium on Smart Control of Turbulence*, pp. 143–148. Center for Smart Control of Turbulence, Tokyo.

- GILLIS, J. C. & JOHNSTON, J. P. 1983 Turbulent boundary-layer flow and structure on a convex wall and its redevelopment on a flat wall. *Journal of Fluid Mechanics* **135**, 123–153.
- GÖRTLER, H. 1954 On the three-dimensional instability of laminar boundary layers on concave walls. *Tech. Rep.* 1375. National Advisory Committee for Aeronautics.
- GUO, Y. & FINLAY, W. H. 1991 Splitting, merging and wavelength selection of vortices in curved and/or rotating channel flow due to Eckhaus instability. *Journal of Fluid Mechanics* **228**, 661–691.
- HAMILTON, J. M., KIM, J. & WALEFFE, F. 1995 Regeneration mechanisms of near-wall turbulent structures. *Journal of Fluid Mechanics* **287**, 317–348.
- HANJALIĆ, K. & LAUNDER, B. E. 1972 Fully developed asymmetric flow in a plane channel. *Journal of Fluid Mechanics* **51** (2), 301–335.
- HARLOW, F. H. & WELCH, J. E. 1965 Numerical calculation of time-dependent viscous incompressible flow of fluid with free surface. *Physics of fluids* **8** (12), 2182.
- HOFFMANN, P. H., MUCK, K. C. & BRADSHAW, P. 1985 The effect of concave surface curvature on turbulent boundary layers. *Journal of Fluid Mechanics* **161**, 371–403.
- HUNT, I. A. & JOUBERT, P. N. 1979 Effects of small streamline curvature on turbulent duct flow. *Journal of Fluid Mechanics* **91** (4), 633–659.
- HUSSAIN, A. K. M. F. 1986 Coherent structures and turbulence. *Journal of Fluid Mechanics* **173**, 303–356.
- HUSSAIN, A. K. M. F. & REYNOLDS, W. C. 1970 The mechanics of an organized wave in turbulent shear flow. *Journal of Fluid Mechanics* **41** (2), 241–258.
- JIMENEZ, J., UHLMANN, M., PINELLI, A. & KAWAHARA, G. 2001 Turbulent shear flow over active and passive porous surfaces. *Journal of Fluid Mechanics* **442**, 89–117.
- KIM, J. & HUSSAIN, F. 1993 Propagation velocity of perturbations in turbulent channel flow. *Physics of Fluids A: Fluid Dynamics* **5** (3), 695–706.
- KIM, J., MOIN, P. & MOSER, R. D. 1987 Turbulence statistics in fully developed channel flow at low Reynolds number. *Journal of Fluid Mechanics* **177**, 133–166.
- KOBAYASHI, M., MAEKAWA, H., TAKANO, T., UCHIYAMA, N., KUBOTA, M. & KOBAYASHI, Y. 1989 Two-dimensional turbulent flow in a curved channel. *JSME international journal. Ser. 2, Fluids engineering, heat transfer, power, combustion, thermophysical properties* **32** (3), 324–331.
- KOUMOUTSAKOS, P. 1999 Vorticity flux control for a turbulent channel flow. *Physics of Fluids* **11** (2), 248–250.
- KRISTOFFERSEN, R. & ANDERSSON, H. I. 1993 Direct simulations of low-Reynolds-number turbulent flow in a rotating channel. *Journal of Fluid Mechanics* **256**, 163–197.
- KUWATA, Y. 2022 Dissimilar turbulent heat transfer enhancement by kelvin-helmholtz rollers over high-aspect-ratio longitudinal ribs. *Journal of Fluid Mechanics* **952**, A21.
- LAADHARI, F. 2002 On the evolution of maximum turbulent kinetic energy production in a channel flow. *Physics of Fluids* **14** (10), L65–L68.
- LEE, M. & MOSER, R. D. 2015 Direct numerical simulation of turbulent channel flow up to. *Journal of Fluid Mechanics* **774**, 395–415.
- LIGRANI, P. M., LONGEST, J. E., KENDALL, M. R. & FIELDS, W. A. 1994 Splitting, merging and spanwise wavenumber selection of dean vortex pairs. *Experiments in fluids* **18**, 41–58.
- LIGRANI, P. M. & NIVER, R. D. 1988 Flow visualization of dean vortices in a curved channel with 40 to 1 aspect ratio. *The Physics of fluids* **31** (12), 3605–3617.
- MAMORI, H. & FUKAGATA, K. 2011 Drag reduction by streamwise traveling wave-like Lorenz force in channel flow. In *Journal of Physics: Conference Series*, , vol. 318, p. 022030. IOP Publishing.
- MATSSON, O. J. E. & ALFREDSSON, P. H. 1990 Curvature-and rotation-induced instabilities in channel flow. *Journal of Fluid Mechanics* **210**, 537–563.
- MATSSON, O. J. E. & ALFREDSSON, P. H. 1992 Experiments on instabilities in curved channel flow. *Physics of Fluids A: Fluid Dynamics* **4** (8), 1666–1676.
- MONTY, J. P., HUTCHINS, N., NG, H. C. H., MARUSIC, I. & CHONG, M. S. 2009 A comparison of turbulent pipe, channel and boundary layer flows. *Journal of Fluid Mechanics* **632**, 431–442.
- MOSER, R. D. & MOIN, P. 1987 The effects of curvature in wall-bounded turbulent flows. *Journal of Fluid Mechanics* **175**, 479–510.
- NAGATA, M. & KASAGI, N. 2004 Spatio-temporal evolution of coherent vortices in wall turbulence with streamwise curvature. *Journal of Turbulence* **5** (1), 017.
- ORLANDI, P. & FATICA, M. 1997 Direct simulations of turbulent flow in a pipe rotating about its axis. *Journal of Fluid Mechanics* **343**, 43–72.

- PATEL, V. C. 1969 Measurements of secondary flow in the boundary layer of a 180 degree curved channel. *Tech. Rep.* ARC CP 1043. Aeronautical Research Council, London.
- PATEL, V. C. & HEAD, M. R. 1969 Some observations on skin friction and velocity profiles in fully developed pipe and channel flows. *Journal of Fluid Mechanics* **38** (1), 181–201.
- PATEL, V. C. & SOTIROPOULOS, F. 1997 Longitudinal curvature effects in turbulent boundary layers. *Progress in Aerospace Sciences* **33** (1–2), 1–70.
- PIROZZOLI, S. 2023 Searching for the log law in open channel flow. *Journal of Fluid Mechanics* **971**, A15.
- PIROZZOLI, S., ROMERO, J., FATICA, M., VERZICCO, R. & ORLANDI, P. 2021 One-point statistics for turbulent pipe flow up to $Re_\tau \approx 6000$. *Journal of Fluid Mechanics* **926**, A28.
- RAMAPRIAN, B. R. & SHIVAPRASAD, B. G. 1978 The structure of turbulent boundary layers along mildly curved surfaces. *Journal of Fluid Mechanics* **85** (2), 273–303.
- RAYLEIGH, J. W. S. 1917 On the dynamics of revolving fluids. *Proceedings of the Royal Society of London. Series A, Containing Papers of a Mathematical and Physical Character* **93** (648), 148–154.
- SMITS, A. J., YOUNG, S. T. B. & BRADSHAW, P. 1979 The effect of short regions of high surface curvature on turbulent boundary layers. *Journal of Fluid Mechanics* **94** (2), 209–242.
- SO, R. M. C. & MELLOR, G. L. 1973 Experiment on convex curvature effects in turbulent boundary layers. *Journal of Fluid Mechanics* **60** (1), 43–62.
- SO, R. M. C. & MELLOR, G. L. 1975 Experiment on turbulent boundary layers on a concave wall. *Aeronautical Quarterly* **26** (1), 25–40.
- THOMAS, A. S. W. & BULL, M. K. 1983 On the role of wall-pressure fluctuations in deterministic motions in the turbulent boundary layer. *Journal of Fluid Mechanics* **128**, 283–322.
- VERZICCO, R. & ORLANDI, P. 1996 A finite-difference scheme for three-dimensional incompressible flows in cylindrical coordinates. *Journal of Computational Physics* **123** (2), 402–414.
- WALLACE, J. M. & BRODKEY, R. S. 1977 Reynolds stress and joint probability density distributions in the u-v plane of a turbulent channel flow. *Physics of Fluids* **20** (3), 351–355.
- WALLACE, J. M., ECKELMANN, H. & BRODKEY, R. S. 1972 The wall region in turbulent shear flow. *Journal of Fluid Mechanics* **54** (1), 39–48.
- WATTENDORF, F. L. 1935 A study of the effect of curvature on fully developed turbulent flow. *Proceedings of the Royal Society of London. Series A-Mathematical and Physical Sciences* **148** (865), 565–598.
- YANG, Y. T. & WU, J. Z. 2012 Channel turbulence with spanwise rotation studied using helical wave decomposition. *Journal of Fluid Mechanics* **692**, 137–152.
- YIMPRASERT, S., KVICK, M., ALFREDSSON, P. H. & MATSUBARA, M. 2021 Flow visualization and skin friction determination in transitional channel flow. *Experiments in Fluids* **62**, 1–16.
- YU, X. & LIU, J. T. C. 1991 The secondary instability in görtler flow. *Physics of Fluids A: Fluid Dynamics* **3** (8), 1845–1847.
- ZANOUN, E. S., NAGIB, H. & DURST, F. 2009 Refined cf relation for turbulent channels and consequences for high-re experiments. *Fluid dynamics research* **41** (2), 021405.
- ZARIPOV, D., LI, R., LUKYANOV, A., SKRYPNIK, A., IVASHCHENKO, E., MULLYADZHANOV, R. & MARKOVICH, D. 2023 Backflow phenomenon in converging and diverging channels. *Experiments in Fluids* **64** (1), 9.